

Song Jinsong

# **On Optimization and Read-out Resolution of the Zero Power Sensor**

**School of Electrical Engineering**

Thesis submitted for examination for the degree of Master of  
Science in Technology.

Espoo 16.9.2012

**Thesis supervisor:**

Prof. Antti Räisänen

**Thesis instructor:**

Docent Ville Viikari

Author: Song Jinsong

Title: On Optimization and Read-out Resolution of the Zero Power Sensor

Date: 16.9.2012

Language: English

Number of pages:8+59

Department of Radio Science and Technology

Professorship: Radio Engineering

Code: S-26

Supervisor: Prof. Antti Räsänen

Instructor: Docent Ville Viikari

Wireless sensors are emerging these days. In certain applications, they reduce installation complexity and maintenance costs. However, there are still limitations with the current passive wireless sensors such as a short detection distance and limited parameters to monitor.

In this thesis work, we further develop a new concept called Zero Power to overcome challenges related to the state-of-art of passive wireless sensors. Zero Power sensor is claimed to exhibit a long read-out distance and being capable to monitor several quantities. The concept utilizes the intermodulation communication principle, in which the sensor reflects a signal which contains sensing information at the intermodulation frequency while illuminated by the reader device at two closely located frequencies.

A wired sensor prototype is fabricated. The sensitivity of the sensor is experimentally characterized and the achievable read-out resolution, which defines the smallest detectable relative change in the sensor capacitance, is theoretically predicted for the first time. After the first prototype, the optimization theory of the sensor circuit is established. Based on the theory, the sensor circuit is optimized to achieve the best resolution. A conjugate matched antenna for the sensor is utilized to reduce the complexity of the sensor circuit and the energy consumption. An optimized sensor with an antenna is manufactured. The sensitivity of the optimized sensor is experimentally characterized and the achievable read-out resolution of the optimized sensor is estimated. Finally, a wireless ECG (Electrocardiography) measurement is demonstrated with the optimized sensor.

According to the experimental results, the sensor can offer 1 % relative resolution (1 % change in the sensor capacitance can be detected) at 13 m distance.

Keywords: Conjugate Matching, Intermodulation Response, Mixers, RFID, Read-out Resolution, Sensitivity, Wireless Sensor

## Preface

This thesis work has been done at VTT, Technical Research Centre of Finland.

I would like to give my gratitude to my instructor Ville Viikari for offering this interesting subject for my Master's thesis and for all the guidance, comments on my thesis as well as my work at VTT.

I would like to thank my supervisor Antti Räisänen not only for the guidance of my thesis, but also for offering a good opportunity to study in Finland.

Juho Heinijoki, Ilkka Marttila, Paula Holmlund, as well as many other colleagues at VTT also deserve my gratitude for helping me during this thesis work. I am also grateful to Professor Pertti Vainikainen for all the help in the last two years. I would like to thank my friends for all the pleasures together.

Finally, I would like to thank my parents for all the support and understanding in my life.

Micronova building, Espoo, 26.8.2012

Song Jinsong

# Contents

|   |            |
|---|------------|
| <b>Abstract</b>   | <b>ii</b>  |
| <b>Preface</b>  | <b>iii</b> |
| <b>Contents</b>   | <b>iv</b>  |
| <b>Symbols and abbreviations</b>  | <b>vi</b>  |
| <b>1 Introduction</b>   | <b>1</b>   |
| 1.1 Wireless sensors overview . . . . .   | 1          |
| 1.1.1 Active sensors . . . . .  | 2          |
| 1.1.2 Semi-passive sensors . . . . .  | 2          |
| 1.1.3 Passive sensors . . . . .   | 3          |
| 1.2 Zero Power project . . . . .  | 7          |
| 1.3 Aims and organization of the thesis . . . . .   | 7          |
| <b>2 Intermodulation read-out principle</b>   | <b>9</b>   |
| 2.1 Intermodulation response of the sensor . . . . .  | 10         |
| <b>3 The first sensor prototypes</b>  | <b>14</b>  |
| 3.1 Equivalent circuit of the sensor . . . . .  | 14         |
| 3.2 Prototypes at 1.2 GHz and 2.1 GHz . . . . .   | 14         |
| 3.3 Measurement setup of the first prototypes . . . . .   | 15         |
| 3.4 Power calibration . . . . .   | 18         |
| 3.4.1 Measurement setup for power calibration . . . . .   | 18         |
| 3.4.2 Calculation of the power calibrated intermodulation response .                            | 19         |
| 3.5 Fitting of the capacitance of the varactor . . . . .  | 20         |
| 3.6 Equation for the relative read-out resolution . . . . .                                     | 21         |
| 3.7 Experiments . . . . .   | 24         |
| 3.7.1 Measured intermodulation response . . . . .   | 24         |
| 3.7.2 Sensitivity of intermodulation response based on the data of<br>the measurement . . . . . | 24         |
| 3.7.3 Theoretical read-out resolution based on the prototype mea-<br>surements . . . . .        | 29         |
| <b>4 Optimization of the sensor platform</b>  | <b>31</b>  |
| 4.1 Optimization of the sensor components values . . . . .                                      | 31         |
| 4.2 Impedance of the optimized sensor . . . . .   | 40         |
| 4.3 Optimization of the sensor antenna . . . . .  | 40         |
| <b>5 Performance of the optimized Zero Power sensor</b>   | <b>44</b>  |
| 5.1 Measurement setup . . . . .   | 44         |
| 5.2 Fitting of the capacitance of the varactor . . . . .  | 44         |
| 5.3 Experiments of the optimized Zero Power sensor . . . . .                                    | 46         |
| 5.3.1 Carrier frequency sweep . . . . .   | 46         |

|          |  |           |
|----------|--|-----------|
| 5.3.2    | Intermodulation response as a function of difference frequency | 46        |
| 5.3.3    | Intermodulation sensitivity . . . . .                          | 48        |
| 5.4      | Read-out resolution . . . . .                                  | 49        |
| 5.5      | ECG measurement . . . . .                                      | 50        |
| <b>6</b> | <b>Conclusion</b>  | <b>54</b> |
|          | <b>References</b>  | <b>55</b> |

# Symbols and abbreviations

## Symbols

|  |   |
|--|---|
| $\gamma$   | Profile parameter for depletion capacitance                             |
| $\lambda$  | Wavelength  |
| $\Phi$   | Built-in potential for diodes   |
| $\omega$   | Angular frequency   |
| $\omega_1, \omega_2$                                   | Carrier angular frequency   |
| $\omega_\Delta$  | Difference angular frequency, $\omega_\Delta = \omega_1 - \omega_2$     |
| $\omega_{IM}$  | Intermodulation angular frequency, $\omega_{IM} = 2\omega_1 - \omega_2$ |
| $a$  | Length of the dipole extension  |
| $b$  | Length of the dipole  |
| $c$  | Width of the loop of the dipole   |
| $C_0, C_q$   | Capacitance of quartz crystal   |
| $C_j(V_j)$   | Junction capacitance at $V_j$   |
| $C_{j0}$   | Junction capacitance at zero bias                                       |
| $C_s$  | Sensor capacitance  |
| $d$  | Thickness of the substrate  |
| $f$  | Frequency   |
| $f_1, f_2, f_{RF}$                                     | Carrier frequency   |
| $f_\Delta$   | Difference frequency, $f_\Delta = f_1 - f_2$                            |
| $f_o$  | Oscillation frequency of quartz crystal                                 |
| $f_{o,\Delta}$   | Difference resonance frequency  |
| $f_{o,RF}$   | Carrier resonance frequency   |
| $f_{IM}$   | Intermodulation frequency, $f_{IM} = 2f_1 - f_2$                        |
| $G_r$  | Reader antenna gain   |
| $G_s$  | Sensor antenna gain   |
| $G_m, G_d, G_s$  | Conductance of circuit  |
| $I_j$  | Current of equivalent Norton current source                             |
| $I_{j,m}$  | Modulated current of equivalent Norton source                           |
| $I_j(\omega_\Delta)$                                   | Current of Norton source at $\omega_\Delta$                             |
| $I_s$  | Saturation current  |
| $k$  | Boltzmann's constant  |
| $L_{RF}, L_\Delta, L_g, L_q$                           | Inductance of circuit   |
| $L_{port1-sensor}, L_{port3-sensor}, L_{sensor-port2}$ | Attenuation of cable  |
| $n$  | Ideality factor   |
| $P_{in}, P_1, P_2$                                     | Input power   |
| $P_{Noise}$  | Noise power   |
| $P_{rad}$  | Power radiated by sensor antenna  |
| $P_{sensor, received}$                                 | Power received by sensor  |
| $P_{sensor, reflected}$                                | Power reflected from sensor   |
| $P_t$  | Transmitted power   |
| $P_{VNA, received}$                                    | Power received by VNA   |

|  |  |
|--|--|
| $P_{VNA,transmitted1}$                       | Power transmitted from port 1 of VNA                   |
| $P_{VNA,transmitted3}$                       | Power transmitted from port 3 of VNA                   |
| $q$  | Elementary charge                                      |
| $Q_j(V_j)$                                   | Charge stored in diode when the bias voltage is $V_j$  |
| $Q_\Delta$                                   | Quality factor of resonance circuit at $\omega_\Delta$ |
| $Q_{RF}$                                     | Quality factor of resonance circuit at $\omega_{RF}$   |
| $Q_m, Q_d, Q_s$                              | Quality factor at low resonance circuit                |
| $R_d$  | Diode resistance                                       |
| $R_g$  | Antenna resistance                                     |
| $R_q$  | Resistance of quartz crystal                           |
| $R_s$  | Junction resistance at zero bias                       |
| $S_{gj}$                                     | Scatter parameter from antenna to mixing diode         |
| $S_{jg}$                                     | Scatter parameter from mixing diode to antenna         |
| $S_{IM}, S_{IM,measured}, S_{IM,calibrated}$ | Scatter parameter of intermodulation response          |
| $T$  | Temperature  |
| $V_j$  | Bias voltage across varactor                           |
| $V_g$  | Voltage across antenna                                 |
| $V_{IM}$                                     | Voltage at intermodulation frequency                   |
| $V_j$  | Voltage across junction of diode                       |
| $V_j(\omega_\Delta)$                         | Voltage across junction of diode at $\omega_\Delta$    |
| $V_j(\omega_{IM})$                           | Voltage across junction of diode at $\omega_{IM}$      |
| $Y_1, Y_{LF}$                                | Admittance of circuit                                  |
| $Z_2, Z_A, Z_N, Z_S$                         | Impedance of circuit                                   |

## Operators

|                                 |  |
|---------------------------------|--|
| $\int dV_j$                     | Integration with respect to $V_j$        |
| $\frac{d}{dt}$                  | Derivation with respect to $t$           |
| $\frac{\partial}{\partial C_s}$ | Partial derivation with respect to $C_s$ |

## Abbreviations

|        |  |
|--------|--|
| AWR    | A circuit simulator, AWR Corporation, 1960 E. Grand Avenue Suite 430 |
| DC     | Direct Current   |
| ECG    | Electrocardiography  |
| Fimecc | Finnish Metals and Engineering Competence Cluster                    |
| FSPL   | Free Space Path Loss   |
| HFSS   | High Frequency Structure Simulator, ANSYS, Inc. Canonsburg, PA 15317 |
| HRV    | Heart Rate Variability   |

|      |                                |
|------|--------------------------------|
| IC   | Integrated Circuit             |
| IM   | Intermodulation                |
| MEMS | Microelectromechanical Systems |
| PCB  | Printed Circuit Board          |
| RFID | Radio Frequency Identification |
| SAW  | Surface Acoustic Wave          |
| SMC  | Scalar Mixer Converter         |
| VNA  | Vector Network Analyser        |
| WSN  | Wireless Sensor Networks       |



# 1 Introduction

## 1.1 Wireless sensors overview

Nowadays, there is an increasing interest in applications of Wireless Sensor Networks (WSN) [1] in various fields, such as environment monitoring [2], building security management [3] and target tracking [4]. Wireless sensors [5] are measurement tools equipped with transceivers to convert signals from sensor elements into a radio transmission. The radio signal is interpreted by a reader device which then converts the wireless signal to a specific desired output, for instance, an analog voltage or a digital signal in a computer. Compared with wired sensors, wireless sensors have several advantages. These include:

- Reduced complexity

Wireless sensor devices can be placed at locations that are challenging to access with a cable because of some specific conditions such as high temperature [6], pressure [7], and hazardous environments. Wireless sensors can also be used in applications where wired read-out is difficult, for instance, due to sealed, moving or rotating parts (See Fig. 1) [8].



Figure 1: Photograph of a tire pressure sensor.

- Reduced installation and maintenance costs

Wireless process control can reduce the cost of monitoring and running a factory by eliminating the need for extension wires, conduits, and other costly accessories. The installation of a wireless sensor system may be less laborious than that of a wired sensor network.

However, wireless sensors also have some drawbacks such as comparatively low speed of communication, limited read-out distance due to attenuation and interference, security issues because of the uncontrollable propagation of signal waves, and limited lifetime of battery-powered sensors.

Wireless sensors are often divided into three categories based on their need for a power source and communication principle.

#### **1.1.1 Active sensors**

Active wireless sensors are equipped with transceivers and are often equipped with a battery. Even a low-power transceiver offers a communication range of up to 100 meters. The price of an active sensor is potentially much higher than that of a passive sensor due to its more complex circuitry [9], and the battery on board limits its life time. Active sensors are applied for example to monitor the active volcano, Reventador, by Harvard University [10], can be used for rapid information retrieval [11], and have been developed towards extending operational lifetimes [12].

#### **1.1.2 Semi-passive sensors**

Semi-passive sensors contain a battery that powers up an IC-circuitry and enables the sensors to operate independently of the reader device or to maintain memory in the sensor. However, the communication with the reader is yet completely passive, no power of the battery is used for transmitting [13]. Relying on the modulated backscattering principle, the sensor simply reflects back some of the power emitted by the reader device. Semi-passive tags can often be used to monitor environmental variables, such as temperature [14], and will be developed to outfit with light [15] and gas concentration [16] sensors.

### 1.1.3 Passive sensors

Passive sensors do not require any power source other than electromagnetic energy from the reader device. Their physical dimensions are small and lifetime long. The advantages of passive sensors over active and semi-passive sensors are that they are potentially more inexpensive and their operation conditions or life-time are not limited by the power source, such as a battery or an energy harvester. The typical reading range is between 10 cm and 3 m [17]. Typical types of passive wireless sensors [18] are RF identification (RFID) [17], surface acoustic wave (SAW) RFID, electrical resonance circuit sensors, harmonic sensors, and intermodulation sensors.

RFID has become commercially significant in recent years and it has replaced barcodes in many identification applications. The advantages of the RFID over barcodes are that no optical line-of-sight is needed and hundreds of tags can be read at a time [20]. RFID uses radio-frequency electromagnetic field to transfer stored

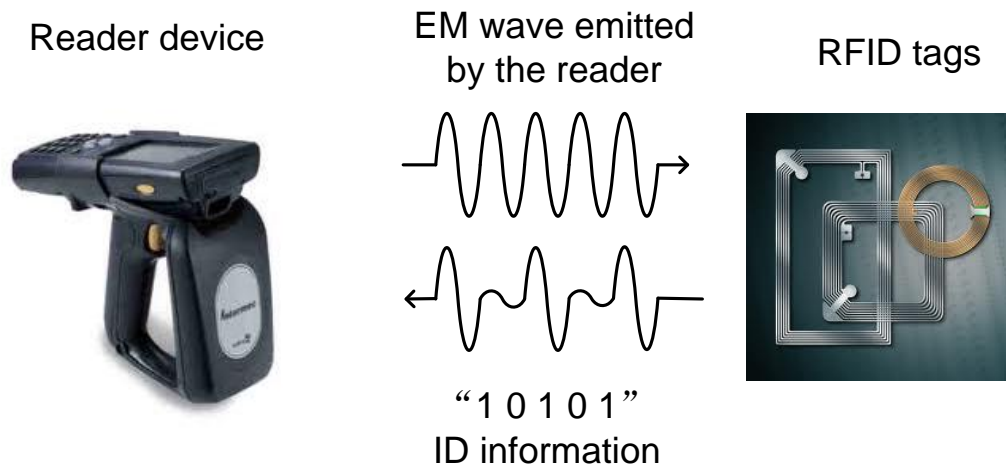


Figure 2: Backscattering communication principle in a RFID system.

identification information from a tag attached to an object. RFID is based on the backscattering communication principle (see Fig. 2). Passive RFID is powered by the electromagnetic field emitted by the reader device and it backscatters the identification information which is stored in the electronic circuit of the tag. The read-out distance, which is limited by the power need of the integrated circuit (IC),

can be up to several metres.

RFID has been widely utilized in industrial automation applications. For example, RFID used in the paper industry would make it possible to identify the individual reels from cradle to grave [21]. RFID attached to an automobile can be used as quality tracking in the assembly line [22]. The focus for developing RFID has been mainly on identification [17], but will increasingly be on other possible applications such as on sensing [23].

A SAW sensor [24] consists of a piezoelectric substrate which supports the metal parts, and a transponder antenna. The operation principle is shown in Fig. 3. The antenna receives the electromagnetic signal and the interdigital transducer applies an electric field to a piezoelectric material which generates surface acoustic waves. The waves propagate over the surface of the piezoelectric crystal and are partly reflected from the reflectors. Then the reflected acoustic waves are converted back to electromagnetic field at the interdigital transducer, and emitted back to the reader device by the transponder antenna. Since the SAW propagation properties of piezo-

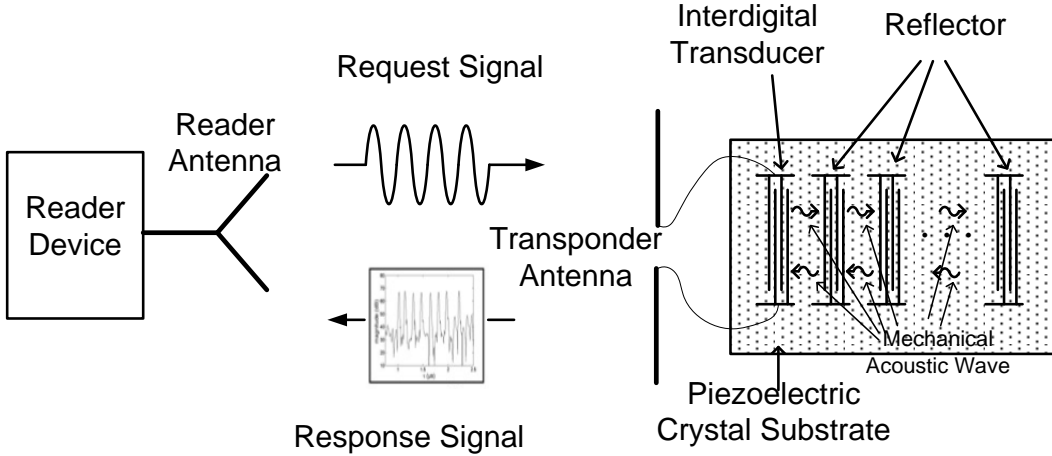


Figure 3: SAW principle.

electric material (e.g. velocity) depend on the physical or chemical quantities such as temperature or pressure, a change of the reflected acoustic wave can be detected correspondingly thus making the sensing possible. SAW sensors have been developed for decades, and have been used in many applications such as non-contact

measurement of temperature, pressure and torque [25]. High sensitivity, intrinsic reliability, and competitive price are the benefits of SAW sensors. Still, the relatively large size and short read-out distance due to high acoustic loss [26] limit their applicability in some cases.

Inductively coupled electrical resonance-circuit sensors are parallel-connected  $LC$  circuits. The inductance or capacitance ( $L_3$  and  $C_2$  in Fig. 4) is sensitive to a physical quantity and therefore the measured quantity also affects the resonance of the sensor [27] [28]. One weakness is that the read-out distance can not be too long

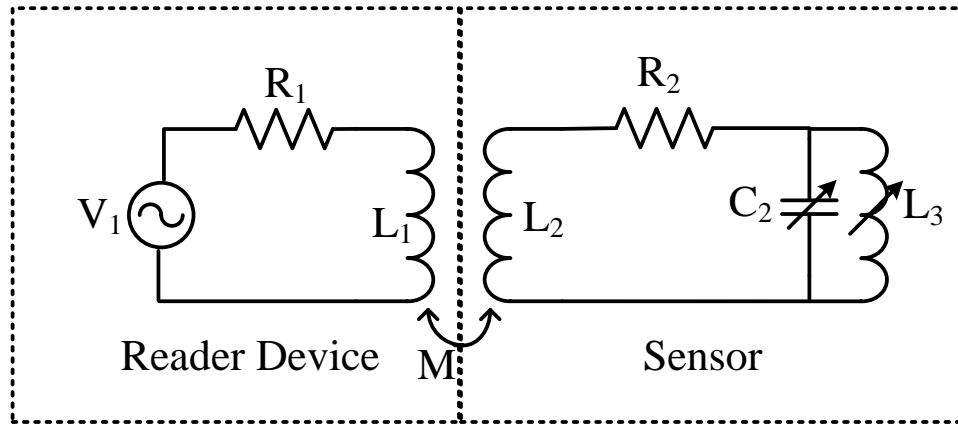


Figure 4: Electrical equivalent circuit for the inductively coupled electrical resonance-circuit sensor.

because of the demand for near-field coupling ( $M$  in Fig. 4) to the reader device. This kind of sensors have been utilized to measure strain [27] and monitor pH [29].

Mixer or harmonic sensors utilize mixing diodes or other elements to generate the sensor response at a harmonic or intermodulation frequency when communicate with a reader device. Although most mixer sensors operate at microwave frequencies, it is declared that improved spatial localization can be obtained by using an optical excitation [30].

Harmonic radar and tags are developed based on the harmonic principle: the tag receives power at the fundamental frequency from the radar device and reflects back the sensor data at a harmonic frequency. As is shown in Fig. 5, a simple harmonic sensor consists of a dipole antenna, a Schottky diode generating harmonic frequencies and an inductive loop to enable the matching between the diode and

antenna such that the highest power of the second harmonic frequency deliver to the dipole antenna [31]. Harmonic sensors were initially developed for automotive

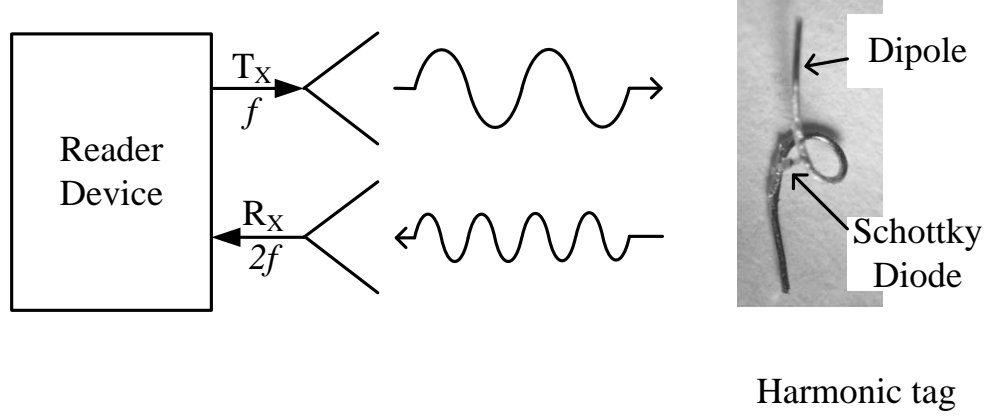


Figure 5: Working principle for harmonic sensors.

vehicles [32] and can provide a good performance for target tracking in a high clutter environment [33]. Harmonic radar and tags have been used to track insects in biological experiments [34] and to find avalanche victims [35].

Intermodulation sensors are harmonic sensors which utilize an intermodulation principle for communication (see Fig. 6). In this principle, the reader transmits a signal containing two frequencies close to each other. The signal, while received by the sensor, is applied to a mixer which generates intermodulation frequencies. The sensor can be designed such, that the intermodulation response is sensitive to a measured quantity. It was first declared that this principle was suitable for telemetry [36] and later was applied to a wireless ferroelectric temperature sensor [37]. Compared with the harmonic principle, the intermodulation principle offers

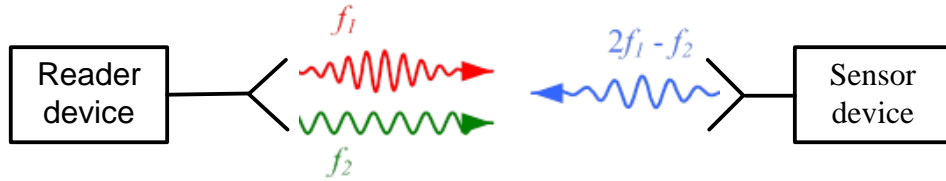


Figure 6: Intermodulation read-out principle.

a smaller frequency offset, which simplifies circuits and antenna design, leading to

smaller sensor size. In general, high carrier frequencies can be used with intermodulation principle and the read-out distance can be longer than that of other passive sensors.

## 1.2 Zero Power project

The work for this thesis has been performed as part of the Zero Power project at VTT, which is a part of Finnish Metals and Engineering Competence Cluster (Fimecc). The aim of this project is to design a new passive, low power consumption sensor network which ensures new systems with significantly reduced life-cycle costs through energy saving, enhanced control of machines and systems, and lower requirement for maintenance. The requirements for Zero Power sensor are

- Wireless operation.
- Low maintenance costs.
- Reliable operation in harsh conditions.
- Low cost of sensor nodes.
- Possibility to monitor several different quantities.

However, the current passive wireless sensors can not meet the objective of the Zero Power project due to the limitations such as: they provide a relatively short detection distance, can be used to monitor only relatively small number of parameters, and are expensive. In this project, a passive wireless sensor utilizing the intermodulation communication principle is developed to meet the objectives.

## 1.3 Aims and organization of the thesis

The purpose of this thesis work is to characterize Zero Power sensors at 866 MHz in terms of read-out resolution and to optimize the sensor platform to obtain the highest sensitivity, and finally to design a matched antenna to achieve the highest possible read-out resolution.

The thesis is organized as follows: Firstly, the principle of intermodulation read-out technologies is introduced in Chapter 2. Secondly, measurement on the performance of the first prototypes based on intermodulation read-out principle is carried out in Chapter 3. Then in Chapter 4, after getting a solid conclusion that this principle works well, a theory of optimization of the sensor is setup, and the sensor is optimized to obtain the best performance. One antenna is designed for the sensor and the sensor performance is measured wirelessly in Chapter 5. Finally, Chapter 6 concludes the work and discusses possibilities for future work on the project.



## 2 Intermodulation read-out principle

The intermodulation read-out principle described in [18] is further illustrated in Fig. 7. The reader device sends two frequencies,  $f_1$  and  $f_2$ , which are close to each other. The two signals received by the sensor antenna (represented as a voltage source) are mixed together in the mixing diode (shown as a varactor in Fig. 7), which generates a current at a difference frequency  $f_\Delta = f_1 - f_2$  as well as other frequencies (e.g.  $f_1 - 2f_2$ ). The current at the intermodulation frequency generated in the diode is represented with a current source in parallel with the diode. The voltage across the diode at the intermodulation frequency depends on the current and the total admittance in parallel with the current generator. The generated signal at the difference frequency further mixes with the original input signals, resulting in the intermodulation frequency  $2f_1 - f_2$ . Since the impedance at the different frequency  $f_\Delta$  is affected by the low-frequency resonance circuit whose resonance impedance is controlled by the sensing element, the voltage at the difference frequency contains the sensor data, and thus the sensor data can be read out by recording the intermodulation response.

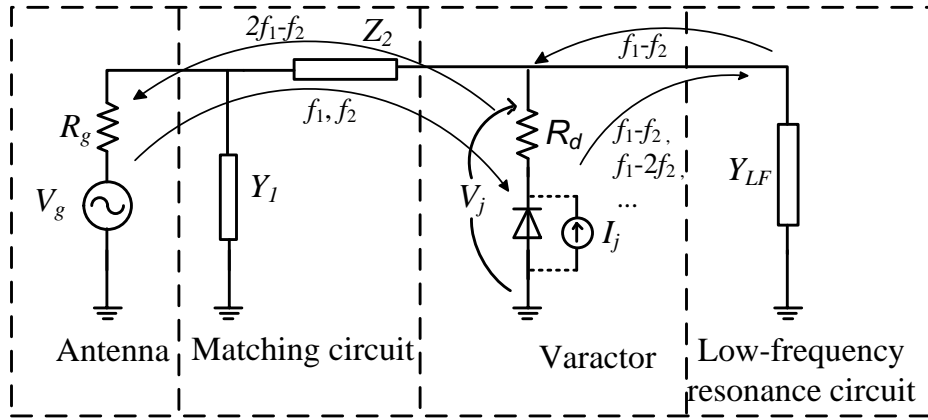


Figure 7: Electrical equivalent circuit of the sensor device.

In the following, a small signal intermodulation response for the sensor is derived following the analysis presentated in [18]. The analytical expression for the response can be utilized to evaluate the measured sensor data. The sensor device typically

consists of four parts: antenna, matching circuit, mixing varactor, and low frequency resonance circuits (see Fig. 7).

## 2.1 Intermodulation response of the sensor

The voltage produced by the antenna is given as

$$\begin{aligned} V_g &= 2\sqrt{2P_{in}R_g}(\sin \omega_1 t + \sin \omega_2 t) \\ &= \hat{V}_g(\sin \omega_1 t + \sin \omega_2 t), \end{aligned} \quad (2.1)$$

where  $P_{in}$  is the power received at each frequency,  $R_g$  represents an antenna resistance,  $\omega_1$  and  $\omega_2$  are the two frequencies emitted by the reader device. Consider the simple equivalent circuit in Fig. 7, the S parameter  $S_{gg}$ , ratio between the voltage of the mixing diode and the voltage across the antenna is given as

$$S_{gg} = \frac{V_j}{V_g} = \frac{Y_d}{j\omega C_{j0}[Z_2(Y_d + Y_{LF}) + 1 + R_g[Z_2 Y_1(Y_d + Y_{LF}) + Y_1 + Y_d + Y_{LF}]]}, \quad (2.2)$$

where  $Y_d = \frac{1}{R_d + \frac{1}{j\omega C_{j0}}}$  is the admittance of the varactor diode in the small signal region,  $C_{j0}$  is the junction capacitance at zero bias, and  $R_d$  is the series resistance of the varactor diode. For a Schottky varactor, the unbiased junction resistance parallel to the diode is typically very large, and can thus be omitted. The junction capacitance as a function of voltage across the varactor is presented as [38]

$$C_j(V_j) = \frac{C_{j0}}{(1 - \frac{V_j}{\Phi})^\gamma}, \quad (2.3)$$

where  $\gamma$  is the profile parameter for the depletion capacitance and  $\Phi$  is a built-in potential. The charge stored in the capacitor is calculated by the integration as

$$Q_j(V_j) = \int C_j(V_j) dV_j = \frac{\Phi C_{j0}}{1 - \gamma} (1 - \frac{V_j}{\Phi})^{-\gamma+1}, \quad (2.4)$$

where a possible constant charge is neglected. The second-order Taylor's approximation for (2.4) is

$$Q_j(V_j) \approx C_{j0}V_j + \frac{\gamma C_{j0}}{2\Phi}V_j^2. \quad (2.5)$$

The current produced by the charge stored in the capacitor can be seen as an equivalent Norton current source (see Fig. 7), which is parallel to the varactor diode,

$$I_j = \frac{dQ_j(V_j)}{dt} = \frac{dC_{j0}V_j}{dt} + \frac{d\gamma C_{j0}V_j^2}{2\Phi dt}. \quad (2.6)$$

Eq. (2.6) could be rewritten as

$$I_j = \frac{dQ_j(V_j)}{dt} \approx j\omega C_{j0}V_j + \frac{\gamma C_{j0}}{2\Phi} \frac{d}{dt}(V_j^2). \quad (2.7)$$

The first term represents the current of a typical voltage-independent capacitor, whereas the second term produces the mixing terms of the two frequencies. The modulated current of the equivalent Norton current source is achieved by substituting (2.1) and (2.2) into (2.7),

$$I_{j,m} \approx \frac{\gamma C_{j0} \hat{V}_g^2}{2\Phi} \frac{d}{dt} (S_{jg}(\omega_1) \sin \omega_1 t + S_{jg}(\omega_2) \sin \omega_2 t)^2. \quad (2.8)$$

Thus the current at the difference frequency  $f_\Delta = f_1 - f_2$  is given as

$$I_j(\omega_\Delta) \approx j\omega_\Delta \frac{\gamma C_{j0} \hat{V}_g^2 S_{jg}(\omega_1) S_{jg}(\omega_2)}{2\Phi} \cos \omega_\Delta t. \quad (2.9)$$

The junction voltage at the difference frequency is given as

$$V_j(\omega_\Delta) \approx j\omega_\Delta \frac{\gamma C_{j0} \hat{V}_g^2 S_{jg}(\omega_1) S_{jg}(\omega_2) Z_N(\omega_\Delta)}{2\Phi} \cos \omega_\Delta t, \quad (2.10)$$

where  $Z_N$  is the impedance of the equivalent Norton current source

$$Z_N = \frac{1}{j\omega C_{j0} + \frac{1}{R_d + \frac{1}{Y_{LF} + \frac{1}{Z_2 + \frac{1}{Y_1 + \frac{1}{R_g}}}}}}. \quad (2.11)$$

The current at the difference frequency then actuates the low frequency resonance circuit and causes a voltage across the diode, which mixes with the fundamental frequencies  $\omega_1, \omega_2$ , producing intermodulation frequencies. The voltage across the diode at the intermodulation frequency  $\omega_{IM} = 2\omega_1 - \omega_2$  is calculated by substituting (2.1), (2.10), and (2.11) into (2.7) as follows:

$$V_j(\omega_{IM}) \approx \frac{\omega_{\Delta} \omega_{IM} \gamma^2 C_{j0}^2 \hat{V}_g^3 S_{jg}^2(\omega_1) S_{jg}(\omega_2) Z_N(\omega_{\Delta}) Z_N(\omega_{IM})}{4\Phi^2} \sin \omega_{IM} t. \quad (2.12)$$

The S parameter  $S_{gj}$  is then calculated as

$$S_{gj} = \frac{V_g}{V_j} = \frac{1}{R_d[Y_1 + 1/R_g + Y_{LF} + Y_{LF}Z_2(Y_1 + 1/R_g)] + Z_2(Y_1 + 1/R_g) + 1}. \quad (2.13)$$

Finally, the intermodulation response  $S_{IM}$  is given as

$$S_{IM} = \frac{V_g(\omega_{IM})}{V_g(\omega_1)} \approx \frac{\omega_{\Delta} \omega_{IM} \gamma^2 C_{j0}^2 \hat{V}_g^2 S_{jg}^2(\omega_1) S_{jg}(\omega_2) S_{gj}(\omega_{IM}) Z_N(\omega_{\Delta}) Z_N(\omega_{IM})}{4\Phi^2}. \quad (2.14)$$

It should be noticed that there are several ways to generate the intermodulation frequency  $2f_1 - f_2$  from Taylor's approximation. Three main ways are shown in Fig. 8. In practice, the current generated by higher order terms and higher number of consecutive mixing processes are weak and neglected. It is declared that the intermodulation currents generated by the first and third processes in Fig. 8 are not important in this application because they are independent from resonance at the low-frequency circuits and the different frequency  $f_{\Delta}$  [18]. The current produced by the second process in Fig. 8 depends on the difference frequency  $(\omega_1 - \omega_2$  in red

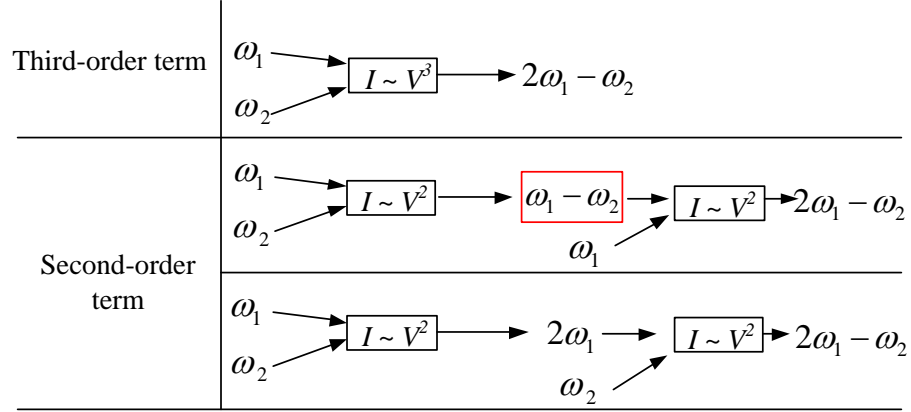


Figure 8: Three different mixing processes that generate an intermodulation frequency.

frame) and can be applied for the sensor read-out.

Applying the previous analysis to the sensor circuit of Fig. 9, an intermodulation response is achieved under the assumption of  $f_\Delta \ll f_{RF}/Q_{RF}$

$$S_{IM} \sim \frac{Q_{RF}^4}{(Q_{RF}^2(\frac{f_{0,RF}^2 - f_{RF}^2}{f_{0,RF}^2}) + \frac{f_{RF}^2}{f_{0,RF}^2})^2} \times \frac{Q_\Delta}{\sqrt{(Q_\Delta^2(\frac{f_{0,\Delta}^2 - f_\Delta^2}{f_{0,\Delta}^2}) + \frac{f_\Delta^2}{f_{0,\Delta}^2})}}, \quad (2.15)$$

where  $Q_{RF} = 1/(2\pi f_{0,RF} R_{RF} C_{j0})$  and  $Q_\Delta = 1/(2\pi f_{0,\Delta} R_\Delta C_{j0})$  are the quality factors of the two resonance circuits at the carrier resonance frequency  $f_{0,RF} = 1/(2\pi\sqrt{L_{RF}C_{j0}})$  and the difference resonance frequency  $f_{0,\Delta} = 1/(2\pi\sqrt{L_\Delta C_{j0}})$ . The

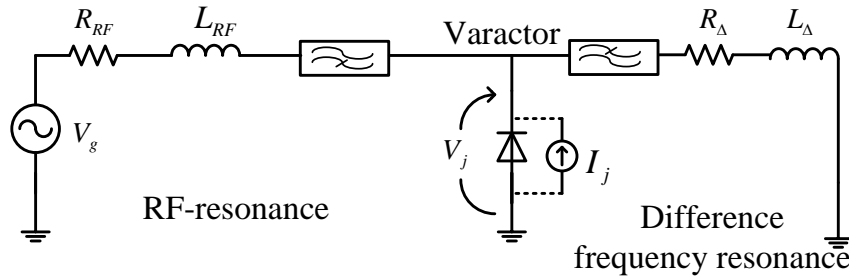


Figure 9: Simplified equivalent circuit of the sensor.

above equation shows that the intermodulation response  $S_{IM}$  is proportional to the quality factor of the low frequency circuit directly. Thus it is important to achieve high quality factors to obtain long read-out distance.

### 3 The first sensor prototypes

#### 3.1 Equivalent circuit of the sensor

A mechanical resonator (quartz-crystal) is used to replace an inductor since quartz crystal resonators tend to exhibit higher quality factor and equivalent inductance for a given self-resonate frequency as compared with electrical inductors [19]. The equivalent circuit with a quartz-crystal is shown in Fig. 10. The capacitive sensor

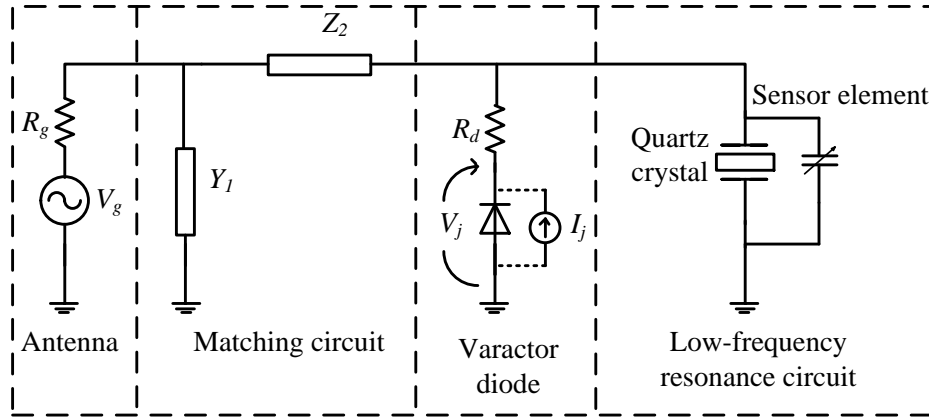


Figure 10: Electrical equivalent circuit for the sensor with a quartz-crystal.

element is aligned in parallel to the crystal in the low frequency resonance circuit such that the capacitance tunes the resonance frequency of the low-frequency circuit and affects the intermodulation response.

#### 3.2 Prototypes at 1.2 GHz and 2.1 GHz

The first prototype sensors were manufactured to experimentally verify the intermodulation response theory. Based on the circuit in Fig. 10, two prototypes were designed and built for 866 MHz and 2.4 GHz frequencies. The photographs of the two prototypes are shown in Fig. 11.

Fig. 12 shows the measured reflection coefficients of the prototypes. The reflection coefficients are measured at a very low power level to ensure the operation in the small signal region. The best matching is obtained at 1.2 GHz and 2.1 GHz. The shifts of the matching frequencies as compared to designed matching frequen-

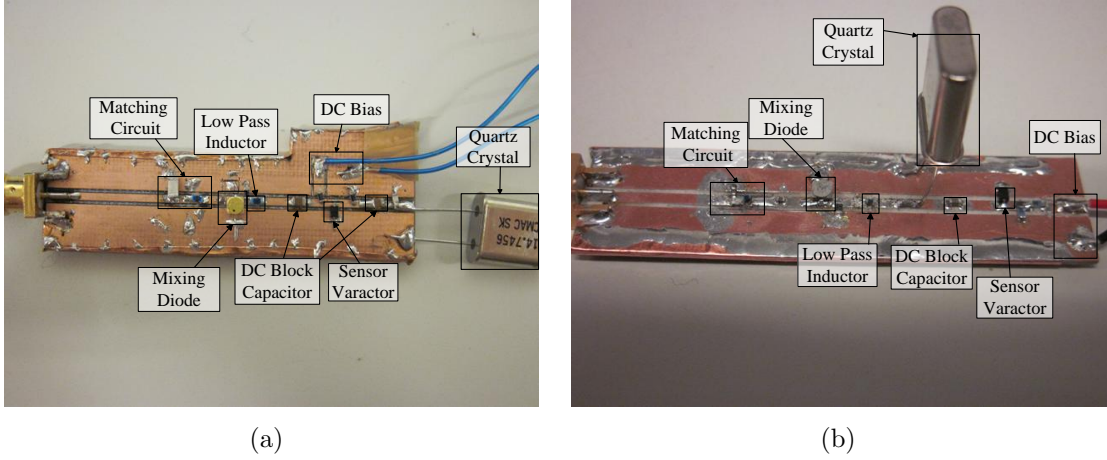


Figure 11: Photographs of the two prototypes for 866 MHz (a) and 2.4 GHz (b).

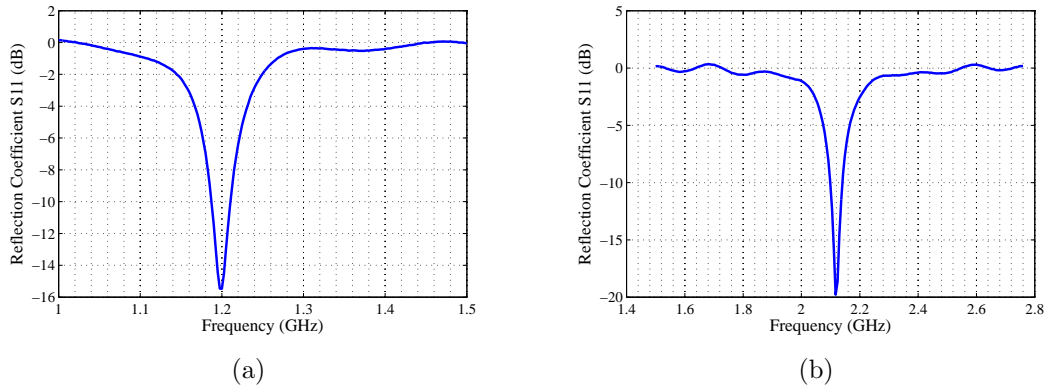


Figure 12: Measured reflection coefficients of the prototypes for 866 MHz (a) and 2.4 GHz (b).

cies are mainly due to the parasitic capacitances of the lumped inductors that were neglected in the AWR simulation, the rounded up components that exist in the designer sample kit, and the alignment inaccuracies in placing the components on the PCB.

### 3.3 Measurement setup of the first prototypes

The intermodulation responses for 1.2 GHz and 2.1 GHz are measured with a network analyser (Agilent, N5245A). The measurement is carried out under SMC Setup (Scalar Mixer Converter) in the menu of *Response* of the VNA. Table 1 shows the measurement frequencies and power for 1.2 GHz and 2.1 GHz prototypes.

Fig. 13 shows the layout of the measurement setup. The fundamental tones

Table 1: Measurement parameters for 1.2 GHz and 2.1 GHz prototypes.

|   |   |   |
|---|---|---|
| 1st Fundamental frequency               | $f_1 = 1.2 \text{ GHz}$                               | $f_1 = 2.1 \text{ GHz}$                               |
| 2nd Fundamental frequency               | $f_2 = 1.21474 \dots$<br>$\dots 1.21476 \text{ GHz}$  | $f_2 = 2.11599 \dots$<br>$\dots 2.11601 \text{ GHz}$  |
| Difference frequency                    | $f_\Delta = 14.74 \dots$<br>$\dots 14.76 \text{ MHz}$ | $f_\Delta = 15.99 \dots$<br>$\dots 16.01 \text{ MHz}$ |
| Oscillation frequency of quartz crystal | $f_o = 14.7456 \text{ MHz}$                           | $f_o = 16.0000 \text{ MHz}$                           |
| Input power                             | $P_1 = P_2 = -11 \text{ dBm}$                         | $P_1 = P_2 = -11 \text{ dBm}$                         |

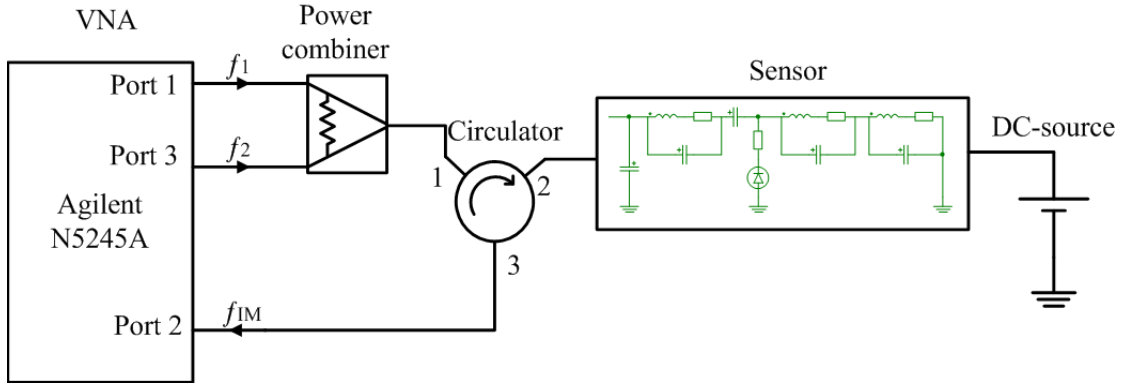


Figure 13: Schematic layout of wired measurement setup for measuring the inter-modulation response of the sensor.

at  $f_1$  and  $f_2$  fed from Port 1 and Port 3 are combined together with the power combiner (Narda, 4321-2 at 1.2 GHz and Narda, 4321-4 at 2.1 GHz), and then fed to the sensor through the circulator (Western Microwave, 3JC-1020 at 1.2 GHz and Ditom, D3C2040 at 2.1GHz). The intermodulation signal reflected from the sensor is fed to Port 2 of the VNA through the circulator.

In this experiment, a varactor (voltage controlled capacitor) is used to represent a capacitive sensor element. A varactor was chosen because its capacitance can be precisely controlled with an external DC-voltage. The varactor is biased by a DC power source whose supply voltage is monitored by the power meter (Agilent 34401A). The wired measurement setup for 1.2 GHz is shown in Fig. 14.



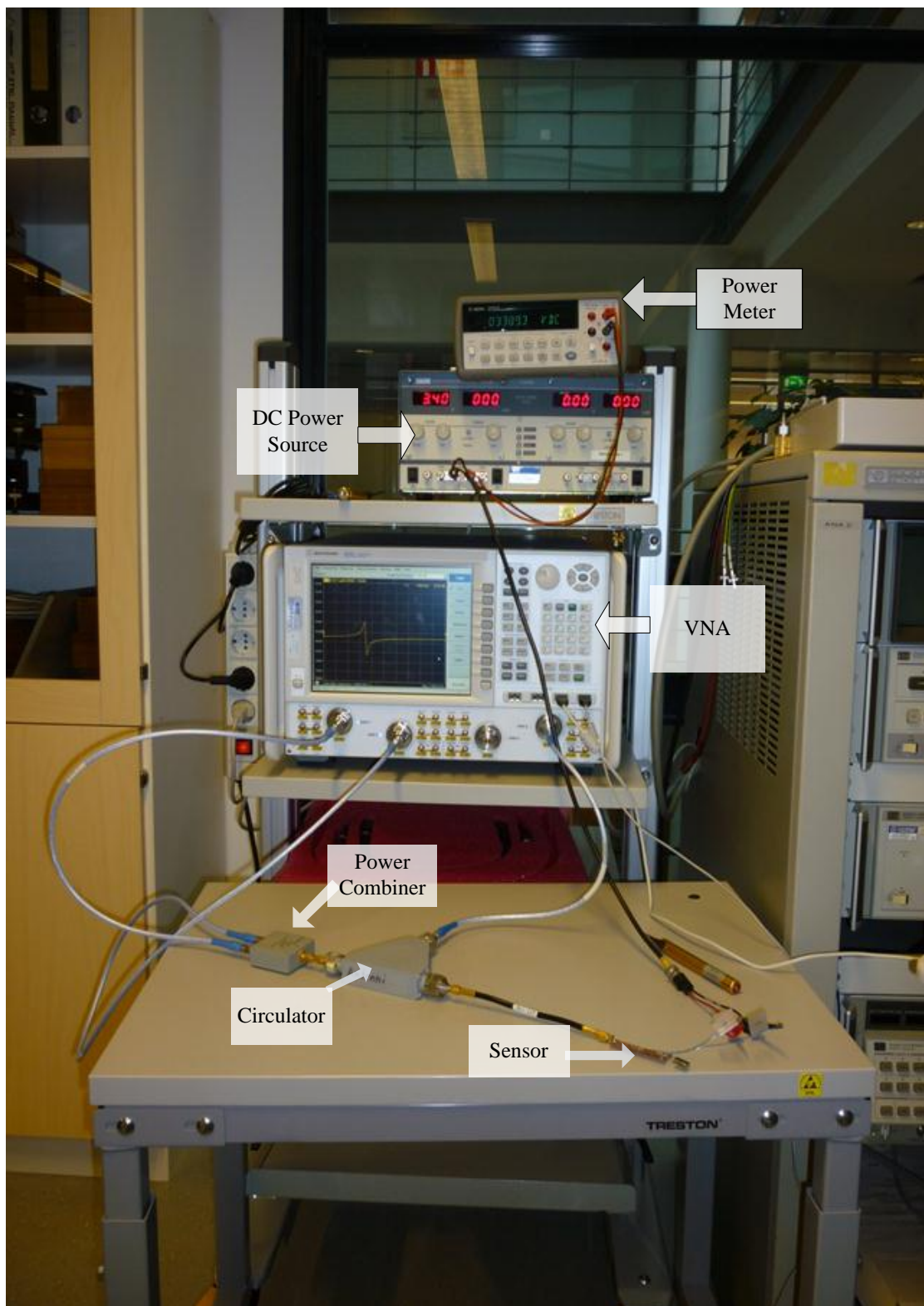


Figure 14: Photograph of the measurement setup for 1.2 GHz.

### 3.4 Power calibration

#### 3.4.1 Measurement setup for power calibration

VNA was calibrated to the SMA-connectors of ports 1, 2 and 3 according to the standard calibration procedure. Power calibration to the sensor was done by post-processing the measured results using the measured attenuation values for the cables, power combiner, and circulator. Phase calibration to the sensor was not performed because absolute phase is not relevant in the experiment.

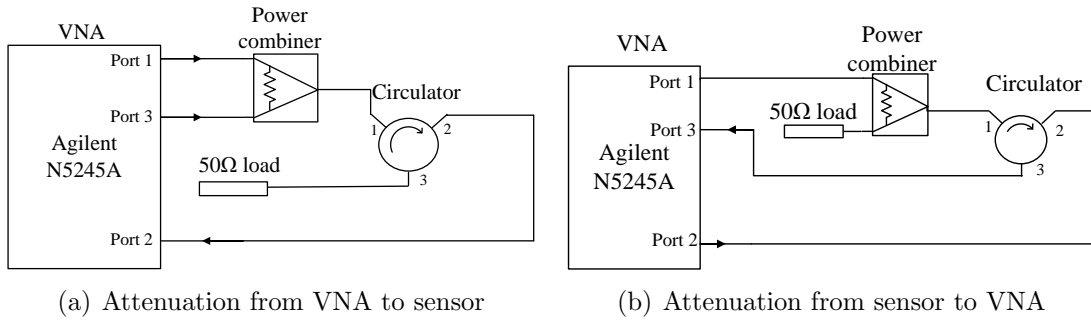


Figure 15: Power calibration setups.

The power calibration setup is shown in Fig. 15. Attenuation from port 1 to sensor  $L_{port1-sensor}$  ( $\frac{1}{S_{21}}$ ) and from port 3 to sensor  $L_{port3-sensor}$  ( $\frac{1}{S_{23}}$ ) are measured from VNA port 1 and 3 to the sensor through the power combiner and circulator respectively using the setup in Fig. 15(a).  $L_{sensor-port2}$  ( $\frac{1}{S_{32}}$ ) is the attenuation of the intermodulation signal reflected from the sensor to the Port 2 of the VNA through the circulator, which is shown in Fig. 15(b). A photograph of the attenuation measurement is given in Fig. 16.

The measured attenuation values are shown in Table 2.

Table 2: Result of the attenuation of the sensor setup.

|          |                     |          |
|----------|---------------------|----------|
| $S_{21}$ | $-L_{port1-sensor}$ | -4.8 dB  |
| $S_{23}$ | $-L_{port3-sensor}$ | -4.9 dB  |
| $S_{32}$ | $-L_{sensor-port2}$ | -0.97 dB |

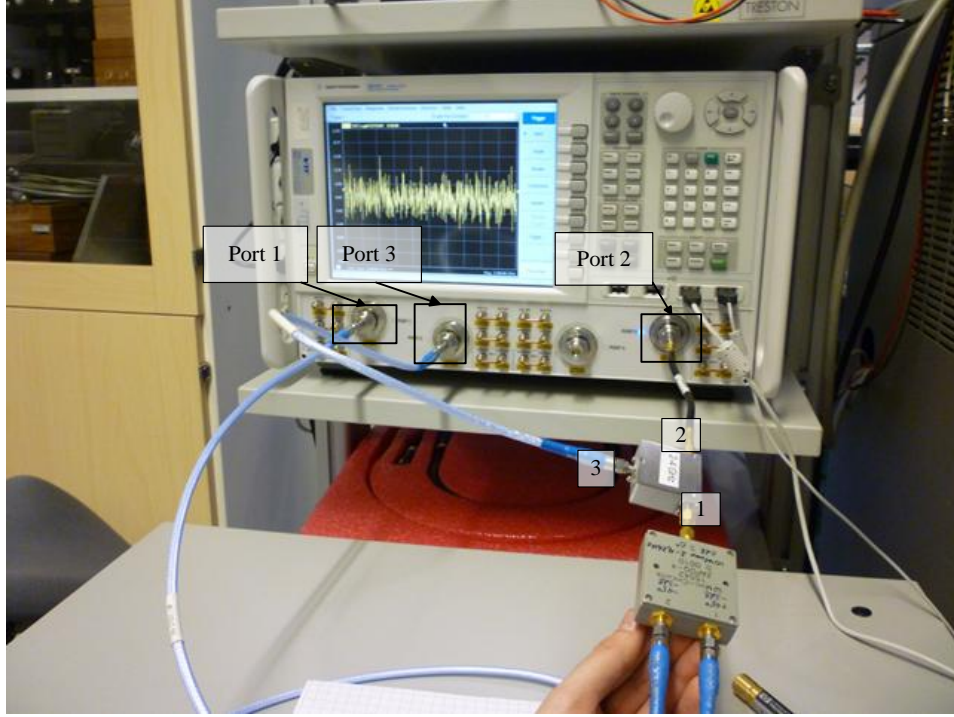


Figure 16: Photograph of the attenuation measurement from sensor to VNA.

### 3.4.2 Calculation of the power calibrated intermodulation response

In the following, we derive an equation for calculating the power calibrated intermodulation (IM) response  $S_{IM,calibrated}$  from the measured intermodulation (IM) response  $S_{IM,measured}$ .

The IM response measured by the VNA is defined as the power received at port 2,  $P_{VNA,received}$ , divided by the power transmitted from port 1,  $P_{VNA,transmitted1}$ , namely

$$|S_{IM,measured}|^2 = \frac{P_{VNA,received}}{P_{VNA,transmitted1}}. \quad (3.1)$$

The calibrated intermodulation response  $S_{IM,calibrated}$  is defined as the power reflected from the sensor,  $P_{sensor,reflected}$ , divided by the power received by the sensor,  $P_{sensor,received}$ ,

$$|S_{IM,calibrated}|^2 = \frac{P_{sensor,reflected}}{P_{sensor,received}}. \quad (3.2)$$

As presented in Table 1, VNA power transmitted from Port 1 and Port 3 are both

-11 dBm,

$$P_{VNA,transmitted1} = P_{VNA,transmitted3} = -11 \text{ dBm}. \quad (3.3)$$

The power received by the sensor is the power transmitted from port 1 and port 3 and attenuated by the setup

$$P_{sensor,received} = \frac{P_{VNA,transmitted1}}{L_{port1-sensor}} + \frac{P_{VNA,transmitted3}}{L_{port3-sensor}}, \quad (3.4)$$

and the power reflected by the sensor is the power received by the VNA and multiplied by the attenuation from the sensor to VNA

$$P_{sensor,reflected} = P_{VNA,received} L_{sensor-port2}. \quad (3.5)$$

The calibrated intermodulation response is obtained by substituting (3.1), (3.3), (3.4) and (3.5) into (3.2)

$$|S_{IM,calibrated}| = |S_{IM,measured}| \sqrt{\frac{L_{sensor-port2}}{\frac{1}{L_{port1-sensor}} + \frac{1}{L_{port3-sensor}}}}. \quad (3.6)$$

### 3.5 Fitting of the capacitance of the varactor

In the measurement, a varactor (NXP Semiconductor, BB149A) is used to represent a capacitive sensor element in the prototype. The intermodulation (IM) responses are measured at different varactor capacitances, which are controlled with an external DC voltage source. The product data sheet [39] specifies some discrete  $C$ - $V$  values. The voltage-dependent junction capacitance of the varactor is assumed to follow [38]

$$C_j(V_j) = \frac{C_{j0}}{(1 + \frac{|V_j|}{\Phi})^\gamma}, \quad (3.7)$$

where  $C_j(V_j)$  is the capacitance when the voltage across the varactor is  $|V_j|$ ,  $C_{j0}$  is the junction capacitance at a zero bias,  $\gamma$  is the profile parameter for the depletion capacitance and  $\Phi$  is a junction potential. A fitted capacitance-voltage curve and

the parameters providing the best fit are shown in Fig. 17.

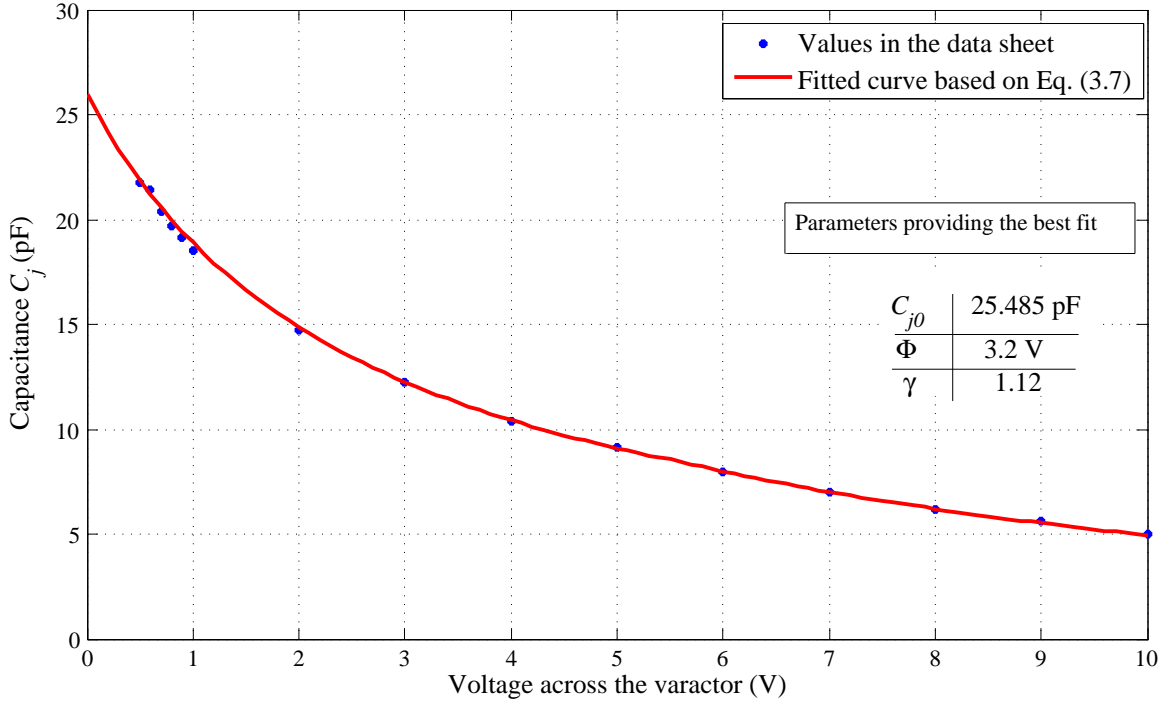


Figure 17: Measured and fitted capacitance as a function of voltage across the varactor.

### 3.6 Equation for the relative read-out resolution

The relative read-out resolution defines the smallest relative change in the sensor capacitance that can be detected by the reader. Ideally, the resolution should be as high as possible to enable accurate measurements across large distances.

The following derives an equation for predicting the read-out resolution from the measured sensitivity of the sensor. According to the Friis free space equation [40], the input power received by the sensor is

$$P_{IN} = P_t G_r G_s \left( \frac{\lambda}{4\pi r} \right)^2, \quad (3.8)$$

where  $P_t$  is the power transmitted by the reader,  $G_r$  is the gain of the reader antenna,

$G_s$  is the gain of the sensor antenna,  $\lambda$  is the wavelength and  $r$  is the distance between the sensor and the reader. The voltage across the antenna at the intermodulation frequency is

$$V_{IM} = |S_{IM}|V_A, \quad (3.9)$$

where  $S_{IM} = \frac{V_{IM}}{V_A}$ ,  $V_A$  is the voltage received by the sensor antenna [18]

$$V_A = 2\sqrt{2R_AP_tG_rG_s}\left(\frac{\lambda}{4\pi r}\right)e^{-j\frac{2\pi r}{\lambda}}(\sin \omega_1 t + \sin \omega_2 t). \quad (3.10)$$

Hence, the power radiated by the sensor antenna at the intermodulation frequency is

$$P_{rad} = \frac{(V_{IM})^2}{2R_A} = 4S_{IM}^2P_tG_rG_s\left(\frac{\lambda}{4\pi r}\right)^2, \quad (3.11)$$

and the power received by the reader antenna at the intermodulation frequency is

$$P_R = 4S_{IM}^2P_tG_r^2G_s^2\left(\frac{\lambda}{4\pi r}\right)^4. \quad (3.12)$$

At the small-signal region, the power at the intermodulation frequency is known to be proportional to the third power of input power

$$P_{IM} \sim P_{IN}^3. \quad (3.13)$$

By substituting the relationship of voltage and power into (3.13), the relationship of voltages at the intermodulation frequency and the input frequency is presented as

$$V_{IM} \sim V_{IN}^3. \quad (3.14)$$

The intermodulation response is obtained by taking (3.14) into account.

$$S_{IM}(P_{IN}) = \frac{V_{IM}}{V_{IN}} \sim V_{IN}^2. \quad (3.15)$$

According to (3.15), the intermodulation response is proportional to the input power:

$$S_{IM}(P_{IN}) \sim P_{IN}. \quad (3.16)$$

The intermodulation response of the prototype is measured at power  $P_{IN}(ref)$ . Taking the power dependence into account, the response for arbitrary power in the small-signal region is given as

$$S_{IM}(P_{IN}) = S_{IM}(ref) \frac{P_{IN}}{P_{IN}(ref)}. \quad (3.17)$$

By substituting (3.8) and (3.17) into (3.12), we obtain the power received by the reader antenna at the intermodulation frequency as

$$P_{R,IM} = 4P_t^3 G_r^4 G_s^4 \left(\frac{\lambda}{4\pi r}\right)^8 \frac{|S_{IM}(ref)|^2}{P_{IN}^2(ref)}. \quad (3.18)$$

The change of the power received at the reader antenna is due to the change of the capacitance of the sensor element:

$$\Delta P_{R,IM} = 4P_t^3 G_r^4 G_s^4 \left(\frac{\lambda}{4\pi r}\right)^8 \frac{1}{P_{IN}^2(ref)} \left| \frac{\partial S_{IM}(ref)}{\partial C_s} \Delta C_s \right|^2. \quad (3.19)$$

Change of the power can be detected only if  $\Delta P_{R,IM}$  is greater than the receiver noise power  $P_{Noise}$ , we get the detection limit by setting

$$\Delta P_{R,IM} = P_{Noise}. \quad (3.20)$$

Substituting Eq.(3.20) into Eq.(3.19), we get

$$\Delta C = \frac{1}{\left| \frac{\partial S_{IM}(ref)}{\partial C_s} \right|} \sqrt{\frac{P_{Noise} P_{IN}^2(ref)}{4P_t^3 G_r^4 G_s^4} \left(\frac{4\pi r}{\lambda}\right)^8}, \quad (3.21)$$

and the relative read-out resolution  $\frac{\Delta C}{C_s}$  is given as

$$\frac{\Delta C}{C_s} = \frac{1}{\left| \frac{\partial S_{IM}(ref)}{\partial C_s} C_s \right|} \frac{P_{IN}(ref)}{2G_r^2 G_s^2} \left( \frac{4\pi r}{\lambda} \right)^4 \sqrt{\frac{P_{Noise}}{P_t^3}}. \quad (3.22)$$

## 3.7 Experiments

### 3.7.1 Measured intermodulation response

Fig. 18 shows intermodulation responses measured under different DC-biases of the sensor varactor. By changing the voltage across the varactor from 0 V to 10 V, at a step of 0.1 V, 100 data samples are obtained.

As the voltage changes from 0 V to 10 V, the capacitance of the varactor changes from 26 pF to 5 pF (see Fig. 17), resulting in the resonance frequency shifting from lower frequency to higher frequency as shown in Fig. 18. The intermodulation response in Fig. 18(b) is not as strong as in Fig. 18(a). The reason might be that when I made this prototype, I mistakenly dropped some solder on the mixing diode. Although most of solder on the mixing diode was cleaned, some solder was still left and made the performance worse.

### 3.7.2 Sensitivity of intermodulation response based on the data of the measurement

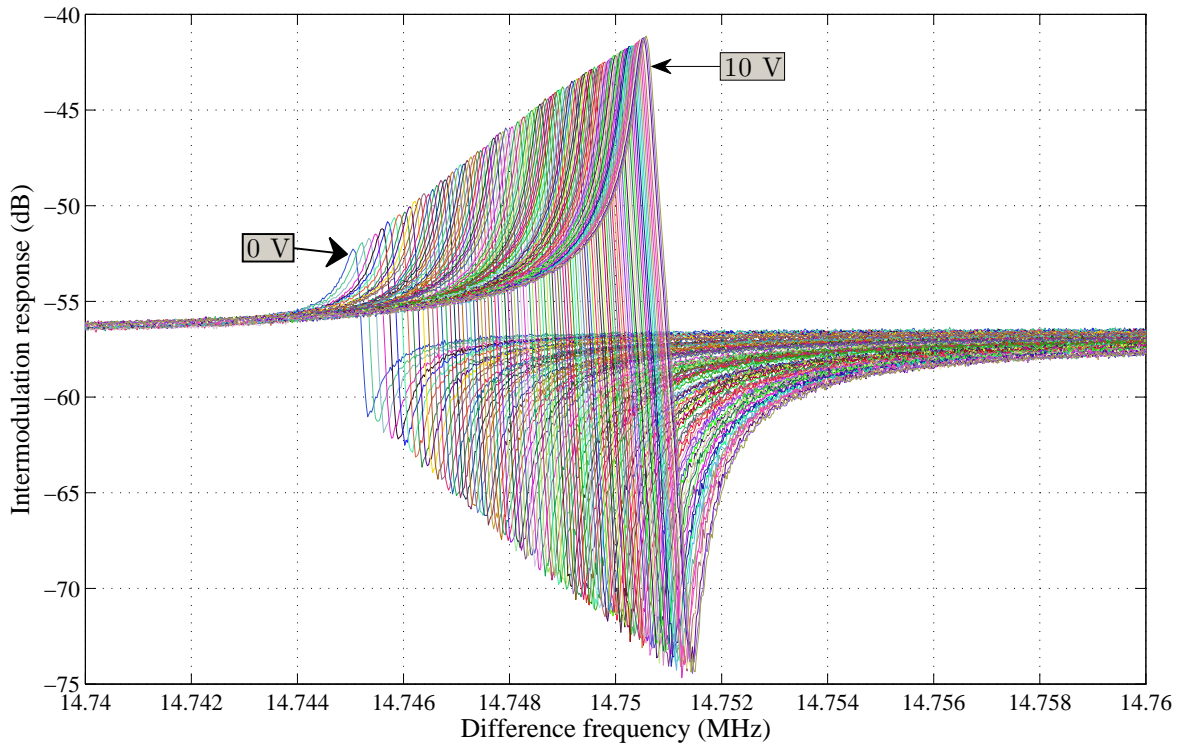
According to (3.22),  $P_{IN}(ref)$ ,  $G_r$ ,  $G_s$ ,  $P_{Noise}$ , and  $P_t$  are the parameters which remain constant once the sensor system is manufactured, and  $\left(\frac{4\pi r}{\lambda}\right)^4$  is the FSPL (Free Space Path Loss) [42] for the signal transmitted and received by the reader device. Hence the relative read-out resolution  $\frac{\Delta C}{C_s}$  is proportional to the reciprocal of the intermodulation sensitivity

$$\frac{\Delta C}{C_s} \sim \frac{1}{\left| \frac{\partial S_{IM}(ref)}{\partial C_s} C_s \right|}. \quad (3.23)$$

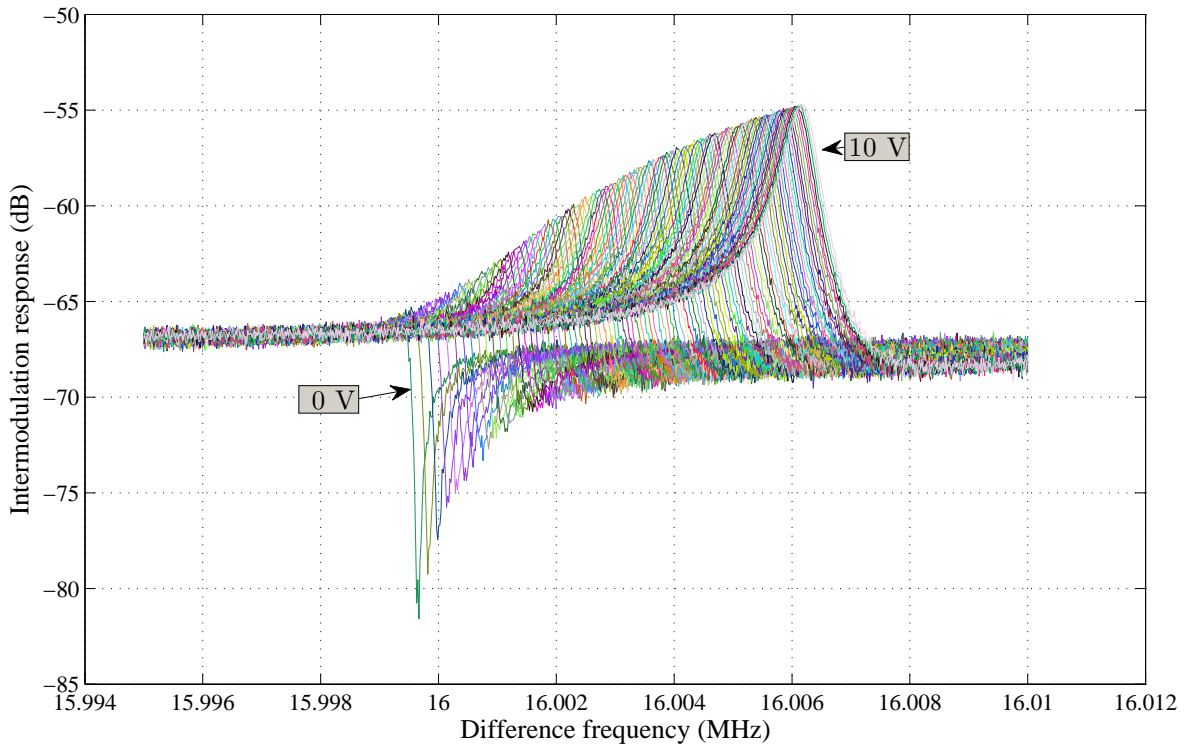
From the 100 data samples for 1.2 GHz and 2.1 GHz prototypes, the intermod-



ulation sensitivity  $|\frac{dS_{IM}(ref)}{dC_s}C_s|$  is calculated and plotted. Fig. 19 is a 2D plot of the intermodulation sensitivity as a function of the voltage across the varactor in  $X$ -axis and the offset from the oscillation frequency of the quartz crystals in  $Y$ -axis. The blue parts of the figure are the areas outside the resonance. As shown in Fig. 19(a) and 19(b), the resonance for both increases with an increasing voltage from 0 V to 10 V, and when the voltage across the varactor is around 9 V, the intermodulation sensitivity  $|\frac{dS_{IM}(ref)}{dC_s}C_s|$  reaches its maximum at its resonance frequency. Fig. 20 shows the intermodulation resolution as a function of capacitance of the varactor. The red curve in the figure shows the maximum intermodulation resolution for each capacitance of the varactor. The blue areas are the collection of all the intermodulation resolution data in Fig. 19.

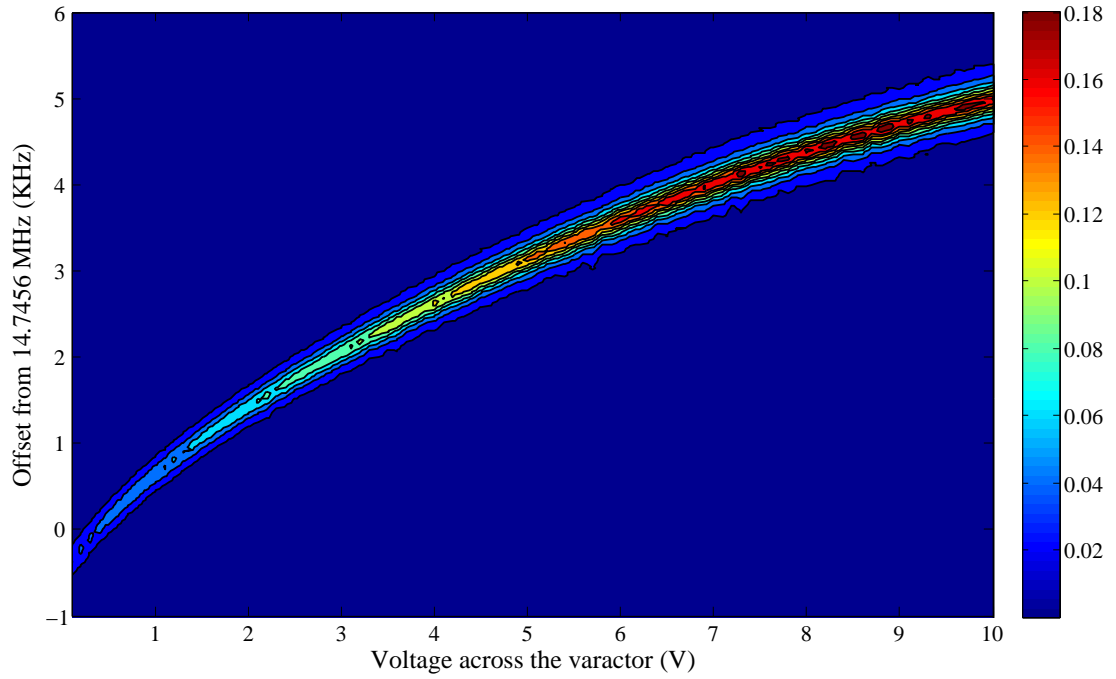


(a) 1.2 GHz

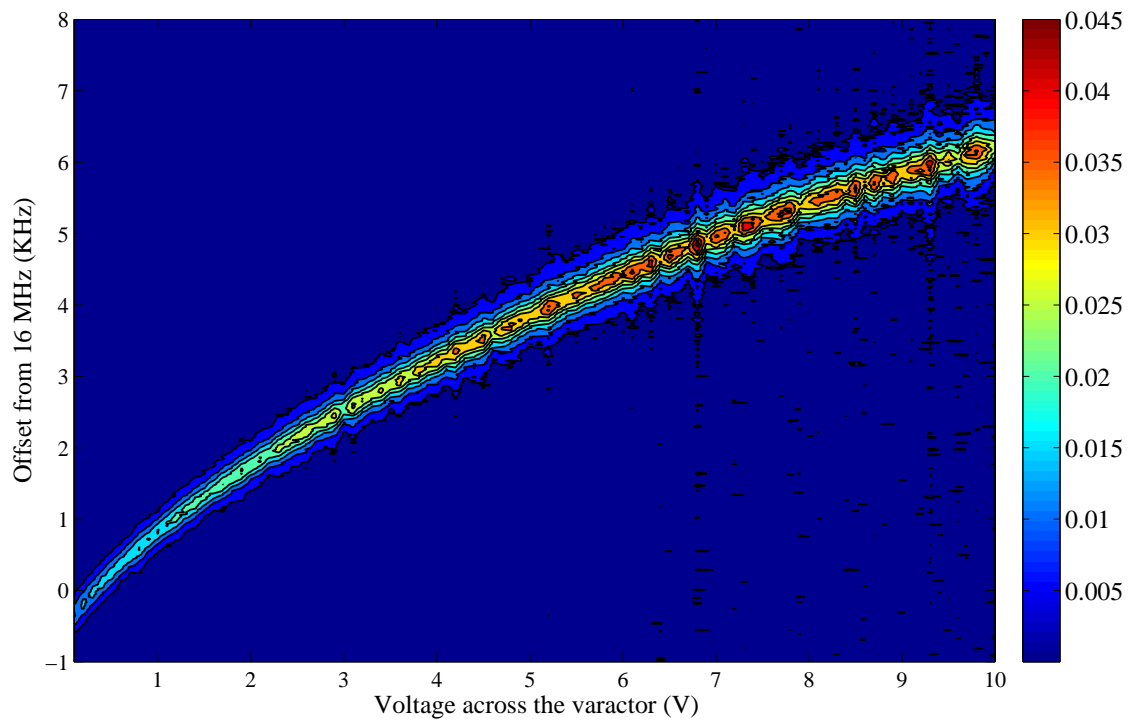


(b) 2.1 GHz

Figure 18: Intermodulation response of different voltages across the varactor.

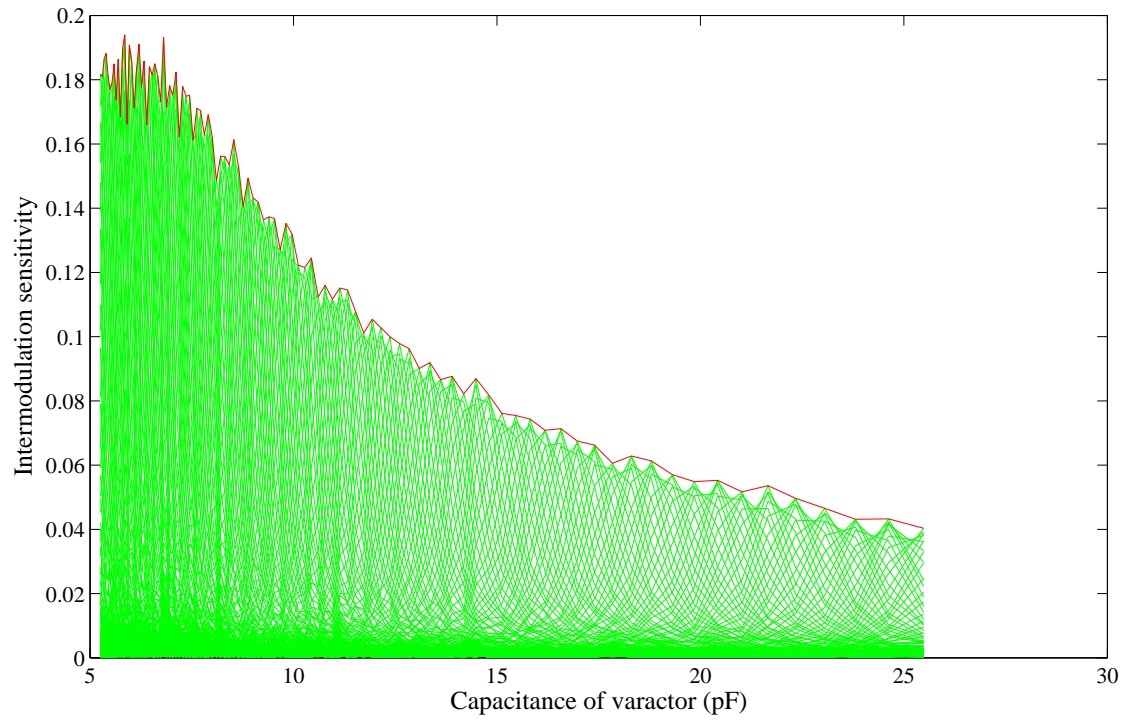


(a) 1.2 GHz

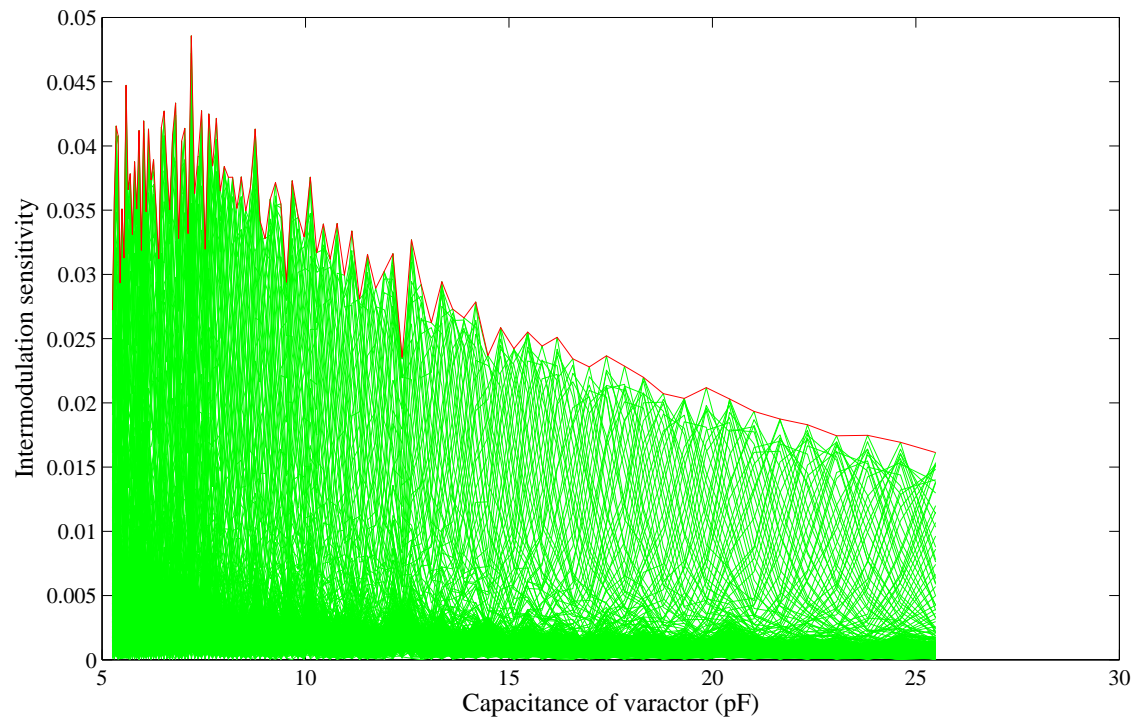


(b) 2.1 GHz

Figure 19: 2D plot of intermodulation sensitivity as a function of the voltage across the varactor ( $X$ -axis) and the offset from the oscillation frequency of the quartz crystals ( $Y$ -axis).



(a) 1.2 GHz



(b) 2.1 GHz

Figure 20: Intermodulation sensitivity as a function of capacitance of the varactor.

### 3.7.3 Theoretical read-out resolution based on the prototype measurements

According to (3.23), the best resolution, or the smallest detectable relative change, is obtained when the intermodulation sensitivity is as high as possible. As shown in Fig. 19 and Fig. 20, the intermodulation sensitivity reaches its maximum when the capacitance is around 7 pF and the voltages around 9 V. The relative read-out resolution can be evaluated based on some typical values for the parameters of the sensor systems.

Since the performance of 2.1 GHz prototype is relatively poor due to the manufacturing process, only the read-out resolution of 1.2 GHz prototype is evaluated. Table 3 gives the parameters for a typical sensor system.

Table 3: Parameters of a sensor system.

|                             |  |
|-----------------------------|--|
| Operating frequency         | $f = 1.2 \text{ GHz}$  |
| Wavelength                  | $\lambda = 0.25 \text{ m}$                                     |
| Transmitted power           | $P_t = 24 \text{ dBm}$   |
| Reader antenna gain         | $G_r = 10 \text{ dBi}$   |
| Sensor antenna gain         | $G_s = 3 \text{ dBi}$  |
| Reference power             | $P_{IN}(ref) = -11 \text{ dBm}$                                |
| Noise power                 | $P_{Noise} = -120 \text{ dBm}$                                 |
| Intermodulation sensitivity | $ \frac{\partial S_{IM}(ref)}{\partial C_s} C_s _{max} = 0.19$ |

By substituting the parameters in Table 3 into (3.22), the typical relative read-out resolution  $\frac{\Delta C}{C_s}$  is obtained and plotted in Fig. 21.

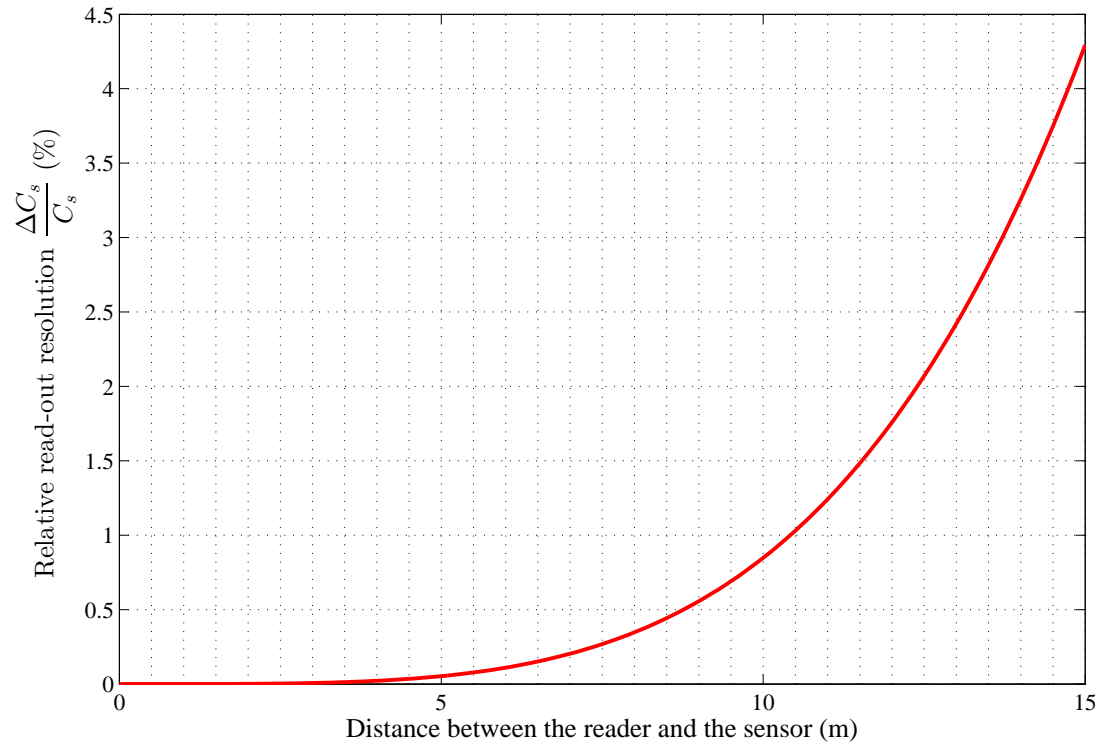


Figure 21: Relative read-out resolution of a typical 1.2 GHz prototype.

The theoretical read-out resolution in Fig. 21 shows that the sensor system is extremely sensitive up to 5 meters (resolution better than 0.1%). When the distance increases up to 10 meters, 1% change of the capacitance can still be detected. Hence, it seems that the intermodulation sensor can offer a large read-out distance and good resolution required in the Zero Power project.

## 4 Optimization of the sensor platform

The objective in this section is to optimize the sensor platform components values and design conjugate matched antenna to the sensor platform (shown as  $Z_A = Z_S^*$  in Fig. 22) to provide the best resolution at 866MHz.

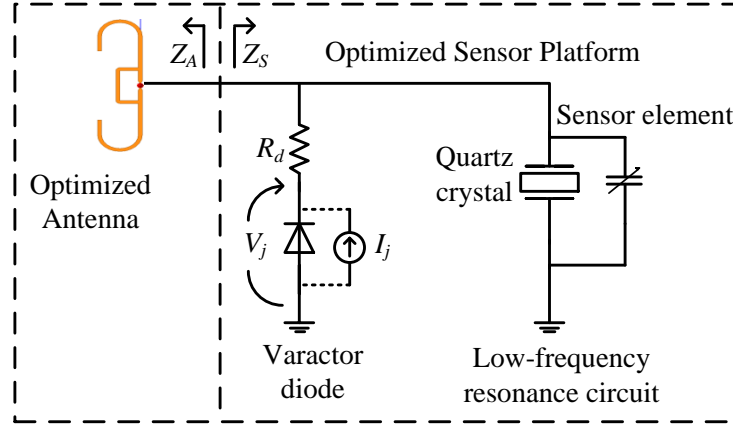


Figure 22: Antenna structure and electrical equivalent circuit for the optimized sensor platform.

### 4.1 Optimization of the sensor components values

Let us consider the equivalent circuit shown in Fig. 23. The voltage backscattered

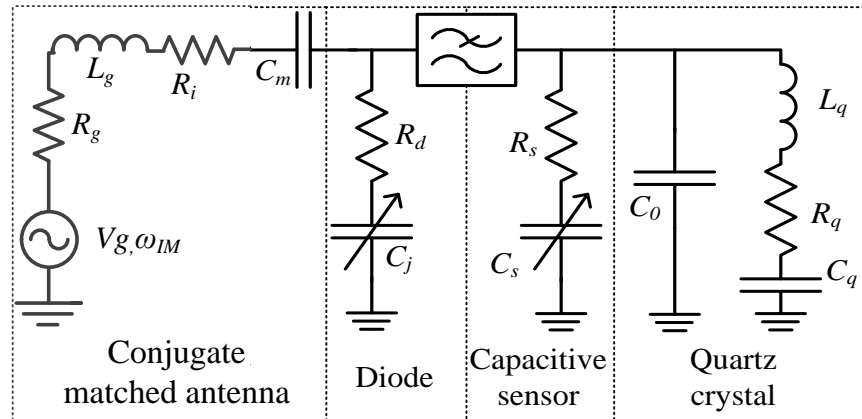


Figure 23: Equivalent circuit for the optimized sensor.

from the sensor platform to the antenna is given as [19]

$$V_{g,\omega_{IM}} = \frac{1}{4}V_g^3 S_{jg}^2(\omega_1) S_{jg}(\omega_2) Z_n(\omega_{IM}) S_{gj}(\omega_{IM}) \left[ \frac{\alpha}{2R_j} + \frac{j\omega_{IM} C_{j0} \gamma (\gamma + 1)}{2\Phi^2} - \frac{\omega_1 \omega_{IM} C_{j0}^2 \gamma^2 Z_n(2\omega_1)}{2\Phi^2} + \left( \frac{\alpha}{R_j} + \frac{j\omega_{\Delta} C_{j0} \gamma}{\Phi} \right) \frac{j\omega_{IM} C_{j0} \gamma Z_n(\omega_{\Delta})}{\Phi} \right] \sin(\omega_{IM} t), \quad (4.1)$$

where  $V_g = 2\sqrt{2P_{IN}R_g}(\sin \omega_1 t + \sin \omega_2 t)$  is the received voltage by the sensor antenna, in which  $P_{IN}$  is the received power at each frequency,  $R_g$  is the antenna impedance,  $S_{jg}$  is the voltage transfer function from antenna to the junction of the diode,  $S_{gj}$  is the voltage transfer function from the junction of the diode to the antenna,  $\alpha = q/nkT$  where  $q$  is the elementary charge,  $n$  is the ideality factor,  $k$  is the Boltzmann's constant and  $T$  is the temperature,  $R_j = 1/\alpha I_s$  is the junction resistance at zero bias,  $I_s$  is a saturation current,  $C_{j0}$  is a junction capacitance at zero bias,  $\gamma$  is the profile parameter, and  $\Phi$  is a junction potential,  $Z_n$  is the impedance across the diode junction. The sensor platform receives the two fundamental frequencies  $\omega_1$  and  $\omega_2$ , and replies at the intermodulation frequency  $\omega_{IM} = 2\omega_1 - \omega_2$ ,  $\omega_{\Delta} = \omega_2 - \omega_1$  is the difference frequency which is close to the resonance frequency of the quartz crystal in Fig. 23. Since the difference frequency  $\omega_{\Delta}$  is so small compared to the carrier frequency, it is assumed that  $\omega_{RF} \approx \omega_1 \approx \omega_2 \approx \omega_{IM}$ . By substituting this and (2.1) into (4.1), the effective output voltage at the intermodulation frequency,  $V_{g,\omega_{IM}}$ , normalized to the antenna resistance, is obtained as

$$\frac{\tilde{V}_{g,\omega_{IM}}}{\sqrt{R_g}} = 4P_{in}^{3/2} R_g S_{jg}^3(\omega_{RF}) Z_n(\omega_{RF}) S_{gj}(\omega_{RF}) \left[ \frac{\alpha}{2R_j} + \frac{j\omega_{RF} C_{j0} \gamma (\gamma + 1)}{2\Phi^2} - \frac{\omega_{RF}^2 C_{j0}^2 \gamma^2 Z_n(2\omega_{RF})}{2\Phi^2} + \left( \frac{\alpha}{R_j} + \frac{j\omega_{\Delta} C_{j0} \gamma}{\Phi} \right) \frac{j\omega_{RF} C_{j0} \gamma Z_n(\omega_{\Delta})}{\Phi} \right], \quad (4.2)$$

Let us consider a capacitive sensor with a relative sensitivity  $\beta$  towards a measured physical quantity  $x$

$$\beta_x = \left( \frac{\delta C_s}{C_s} \right) / \left( \frac{\delta x}{x} \right), \quad (4.3)$$

where  $C_s$  is the capacitance of the sensor. Let us further assume that a sensor



capacitance only affects  $Z_n(\omega_\Delta)$  in (4.2). The voltage change at the intermodulation frequency due to the change in the measure physical quantity is

$$\begin{aligned} \frac{\Delta \tilde{V}_{g,\omega_{IM}}}{\sqrt{R_g}} &= \frac{\delta \tilde{V}_{g,\omega_{IM}}}{\sqrt{R_g} \delta C_s} \frac{\beta_x C_s}{x} \Delta x = \\ &- 4P_{in}^{3/2} R_g S_{jg}^3(\omega_{RF}) Z_n(\omega_{RF}) S_{gj}(\omega_{RF}) \frac{\omega_\Delta \omega_{RF} C_{j0}^2 \gamma^2}{\Phi^2} \frac{\delta Z_n(\omega_\Delta)}{\delta C_s} C_s \beta_x \frac{\Delta x}{x}, \end{aligned} \quad (4.4)$$

where the capacitive nonlinearity is assumed to contribute much more to the mixing than the resistive nonlinearity, which means

$$\frac{\alpha}{R_j} \ll \frac{\omega_\Delta C_{j0} \gamma}{\Phi}. \quad (4.5)$$

The expression of (4.4) can be used to predict an achievable read-out resolution of the sensor and for optimizing the sensor structure.

Consider the simplified electrical equivalent circuit for the sensor shown in Fig. 23. The sensor is connected with a conjugate matched antenna whose internal resistance is  $R_g$  and inductance is  $L_g$ . Resistance  $R_i$  represents losses of the matching inductance  $L_g$ , and  $C_m$  is used as a high pass filter.  $R_d$  represents losses of the total dissipations of the diode. An ideal low pass filter is assumed to prevent RF signal from accessing to the quartz crystal and sensor element.

Obviously, the highest sensitivity is achieved when the antenna is matched to the losses of the matching circuit and the diode, which is,

$$R_g = R_i + R_d, \quad (4.6)$$

$$j\omega_{RF} L_g + \frac{1}{j\omega_{RF} C_m} + \frac{1}{j\omega_{RF} C_j} = 0 \Rightarrow L_g = \frac{C_m + C_j}{\omega_{RF}^2 C_m C_j}. \quad (4.7)$$

The current of the circuit  $I$  is calculated as

$$I = \frac{V_g}{R_g + R_i + R_d}, \quad (4.8)$$

and the voltage across the diode  $C_j$  is presented as

$$V_j = \frac{I}{j\omega_{RF}C_j}. \quad (4.9)$$

The voltage transfer function  $S_{jg}$  is defined as

$$S_{jg} = \frac{V_j}{V_g}. \quad (4.10)$$

Since the resistance of the inductance can be presented by its quality factor  $Q_m$

$$R_i = \frac{\omega_{RF}L_g}{Q_m}, \quad (4.11)$$

the voltage transfer function  $S_{jg}$  can be calculated by substituting (4.6), (4.7), (4.8), (4.9), and (4.11) into (4.10)

$$S_{jg} = \frac{V_g}{2\left(\frac{C_j + C_m}{C_j C_m} + \frac{1}{Q_m}\right)}, \quad (4.12)$$

where  $Q_d = \frac{1}{\omega_{RF}C_j R_d}$  is the quality factor of the diode.

Now let us consider the circuit at the RF frequency. Since a perfect low pass filter in Fig. 23 is assumed to simplify the analysis, the electrical equivalent circuit shown in Fig. 24 is obtained.

The impedance of the equivalent Norton source is given as

$$Z_n = \frac{1}{j\omega C_j + \frac{1}{R_d + R_i + R_g + j\omega L_g + \frac{1}{j\omega C_m}}}, \quad (4.13)$$

the impedance of the backscatter circuit (shown in Fig. 24) is given as

$$Z_b = R_g + j\omega L_g + R_d + R_i + \frac{1}{j\omega C_m}, \quad (4.14)$$

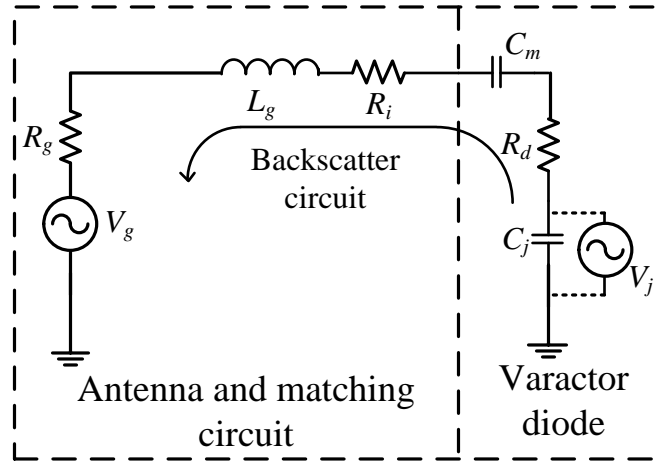


Figure 24: Equivalent circuit at RF frequency  $\omega_{RF}$ .

and the current  $i_b$  on the backscatter circuit is calculated as

$$i_b = \frac{V_j}{Z_b}. \quad (4.15)$$

Thus the voltage backscattered from the diode to the antenna is

$$V_g = i_b R_g. \quad (4.16)$$

Taking (4.6), (4.7), (4.13), (4.14), (4.15), and (4.16) into consideration, the voltage transfer function with the impedance of the Norton source  $S_{jg}Z_N$  can be derived as

$$\begin{aligned} S_{jg}Z_n &= \frac{V_g}{V_j}Z_n \\ &= \frac{R_g}{j\omega C_j(R_g + R_i + R_d) - \frac{C_j + C_m}{C_m} + \frac{C_j}{C_m} + 1} \\ &= \frac{1}{2j\omega C_j}. \end{aligned} \quad (4.17)$$

Since the received signal by the antenna is so small that the sensor works at the

small signal range,  $C_j$  can be considered approximately equal to  $C_{j0}$

$$C_j \approx C_{j0}. \quad (4.18)$$

Hence, by taking (4.12), (4.19), and (4.18) into account, equation (4.4) can be rewritten as

$$\frac{\Delta \tilde{V}_{g,\omega_{IM}}}{\sqrt{R_g}} = \frac{jP_{in}^{3/2}}{4} \frac{1}{\left(\frac{C_j + C_m}{C_m Q_m} + \frac{1}{Q_d}\right)^2} \frac{\omega_{\Delta} \gamma^2}{\omega_{RF} \Phi^2} \frac{\delta Z_n(\omega_{\Delta})}{\delta C_s} C_s \beta_x \frac{\Delta x}{x}. \quad (4.19)$$

The equivalent circuit at the difference frequency  $\omega_{\Delta}$  is shown in Fig. 25. To simplify

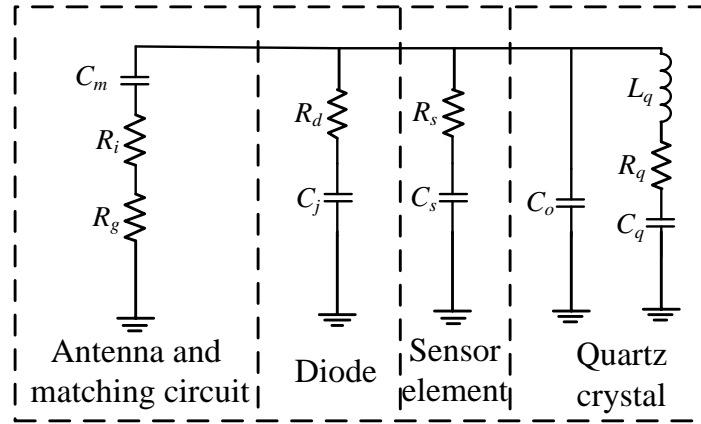


Figure 25: Equivalent circuit at difference frequency  $\omega_{\Delta}$ .

the circuit analysis, the equivalent circuit in Fig. 25 can be transformed to a circuit which only consists of parallel components if the capacitances and quality factors remain the same. The transformed equivalent circuit is shown in Fig. 26. The

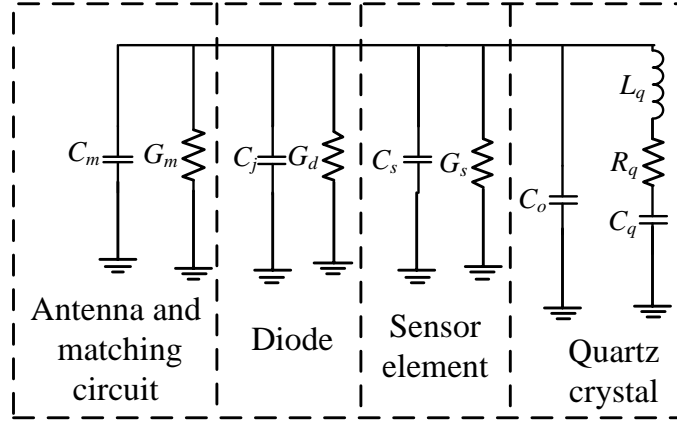


Figure 26: Transformed equivalent circuit at difference frequency  $\omega_\Delta$ .

admittance  $Y_n$  of the circuit in Fig. 26 can be written as

$$\begin{aligned}
 Y_n(\omega_\Delta) &= j\omega_\Delta(C_m + C_j + C_s + C_o) + G_m + G_d + G_s + \frac{1}{R_q + j\omega_\Delta L_q + \frac{1}{j\omega_\Delta C_q}} \\
 &= j\omega_\Delta(C_m + C_j + C_s + C_o) + \frac{\omega_\Delta C_m}{Q_m} + \frac{\omega_\Delta C_j}{Q_d} + \frac{\omega_\Delta C_s}{Q_s} + \frac{R_q - j(\omega_\Delta L_q - \frac{1}{\omega_\Delta C_q})}{R_q^2 + (\omega_\Delta L_q - \frac{1}{\omega_\Delta C_q})^2}.
 \end{aligned} \tag{4.20}$$

$Y_n(\omega_\Delta)$  is real at the resonance frequency:

$$\omega_\Delta(C_m + C_j + C_s + C_o) - \frac{(\omega_\Delta L_q - \frac{1}{\omega_\Delta C_q})}{R_q^2 + (\omega_\Delta L_q - \frac{1}{\omega_\Delta C_q})^2} = 0, \tag{4.21}$$

so  $Y_n$  can be rewritten as

$$Y_n(\omega_\Delta) = \frac{\omega_\Delta C_m}{Q_m} + \frac{\omega_\Delta C_j}{Q_d} + \frac{\omega_\Delta C_s}{Q_s} + \frac{R_q}{R_q^2 + (\omega_\Delta L_q - \frac{1}{\omega_\Delta C_q})^2}. \tag{4.22}$$

Assume  $\omega L_q - \frac{1}{\omega C_q} \gg R_q$ , and substituting this into (4.21) and (4.22), the admit-

tance  $Y_n$  is given as

$$Y_n(\omega_\Delta) = \frac{\omega_\Delta C_m}{Q_m} + \frac{\omega_\Delta C_j}{Q_d} + \frac{\omega_\Delta C_s}{Q_s} + R_g \omega_\Delta^2 (C_m + C_j + C_s + C_o)^2. \quad (4.23)$$

The term  $\frac{\delta Z_n(\omega_\Delta)}{\delta C_s}$  in (4.19) can be represented by  $Y_n$

$$\frac{\delta Z_n(\omega_\Delta)}{\delta C_s} = \frac{\delta(1/Y_n(\omega_\Delta))}{\delta C_s} = -\frac{j\omega_\Delta + \frac{\omega_\Delta}{Q_s}}{Y_n^2} \approx -\frac{j\omega_\Delta}{Y_n^2}. \quad (4.24)$$

Finally, by substituting (4.23) and (4.24) into (4.19), we obtain

$$\begin{aligned} \frac{\Delta \tilde{V}_{g,\omega_{IM}}}{\sqrt{R_g}} &= \frac{P_{in}^{3/2}}{4} \frac{1}{\left(\frac{C_j + C_m}{C_m Q_m} + \frac{1}{Q_d}\right)^2} \\ &\quad \frac{C_s}{\left(\frac{C_m}{Q_m} + \frac{C_j}{Q_d} + \frac{C_s}{Q_s} + R_g \omega_\Delta (C_m + C_j + C_s + C_o)^2\right)^2} \frac{\gamma^2}{\omega_{RF} \Phi^2} \beta_x \frac{\Delta x}{x}. \end{aligned} \quad (4.25)$$

This equation can be used to maximize the read out sensitivity by optimizing the capacitances when the quality factors of different components are given.

According to (4.25), the highest sensitivity is achieved when  $C_j$  approaches zero. This is because we neglected parasitic capacitance in parallel with the junction and assumed a conjugate match between the antenna and the diode. Hence, we first fix the junction capacitance and then optimize  $C_m$ ,  $C_s$ , and  $C_o$  to get the highest sensitivity. The junction capacitance should be selected so that a low-loss conjugate matching can be realized at the desired carrier frequency.

The optimized circuit based on (4.25) is shown as Fig. 27. The elements have already been rounded to closest available component values. The elements are arranged symmetrically in this circuit such that the sensor can be biased using differential input to improve interference rejection in tests in the anechoic chamber. The 2 pF capacitors are used as high pass filter which allow the RF signals transmit between the sensor platform and antenna and block the low frequency signal from transmitting back to the antenna directly. The 470 nH inductors are used as low pass filters to prevent RF signal accessing the crystal. The 330 pF capacitors act

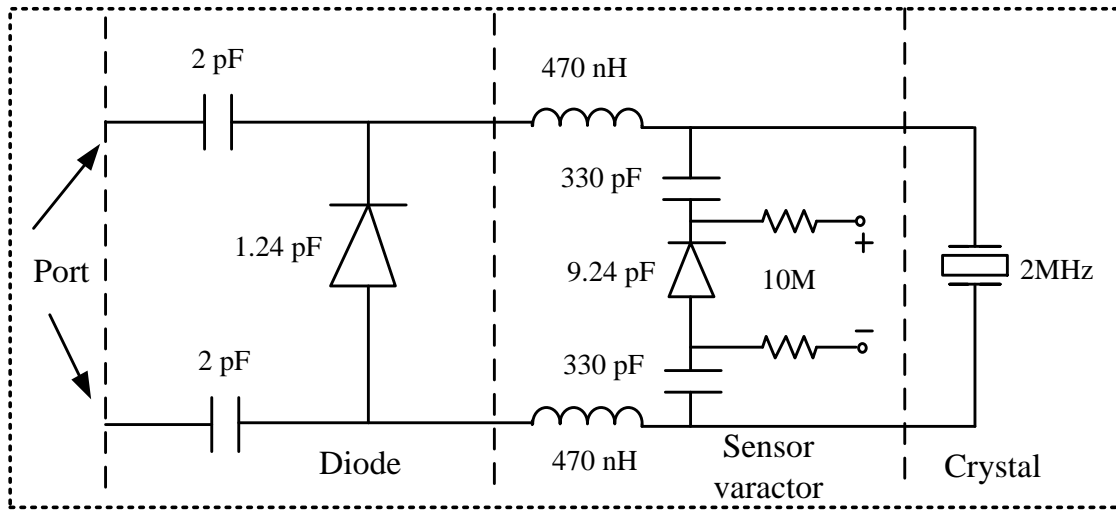


Figure 27: Achievable optimized equivalent circuits for Zero Power sensor.

as DC blocks. Two  $10\text{ M}\Omega$  resistors are used to block the large capacitance in the DC source. SKYWORKS SMV1430-079LF is chosen as the mixing diode because a low-loss conjugate matching is straightforward to realize at the carrier frequency. Based on Fig. 27, a prototype of the sensor platform is manufactured. A photograph is shown in Fig. 28.

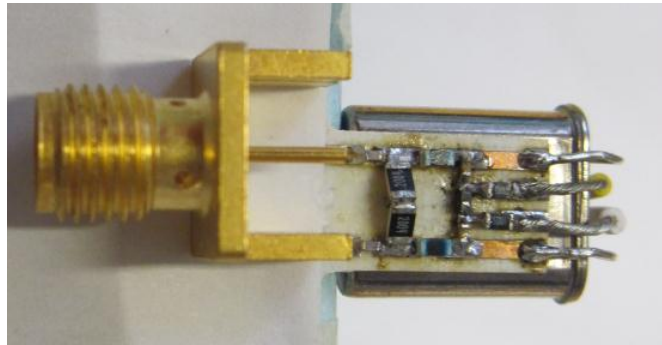


Figure 28: Photograph of the Zero Power sensor platform.

## 4.2 Impedance of the optimized sensor

The impedance of the sensor platform in Fig. 28 is measured using the VNA. Three calibration standards are used to shift the reference plane to the antenna feed (shown in Fig. 29). The measured sensor impedance after the calibration is  $13.3-j214 \Omega$  at

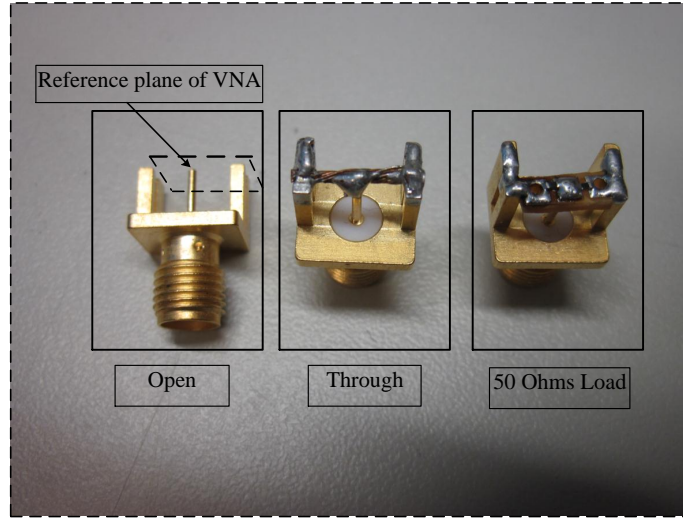


Figure 29: Photograph of the calibration standards.

866 MHz.

## 4.3 Optimization of the sensor antenna

Generally, to maximize the power delivered between the antenna and sensor platform, an antenna is designed to be conjugate matched to the impedance of sensor platform so that separate matching circuits are not needed [43]. Hence, the antenna impedance should be  $13.3+j214 \Omega$  at 866 MHz.

Inductive antennas are mainly studied and used in RFID tags [44]. One possible antenna structure is shown in Fig. 30. The loop in the antenna structure contributes to inductance. By adjusting the length of the dipole  $a$  and  $b$ , and the length of the loop  $c$  in Fig. 30, the objective impedance can be achieved. The antenna simulation is carried out in HFSS 14.0, and ROGERS RO4359B is used as the substrate for the antenna structure.



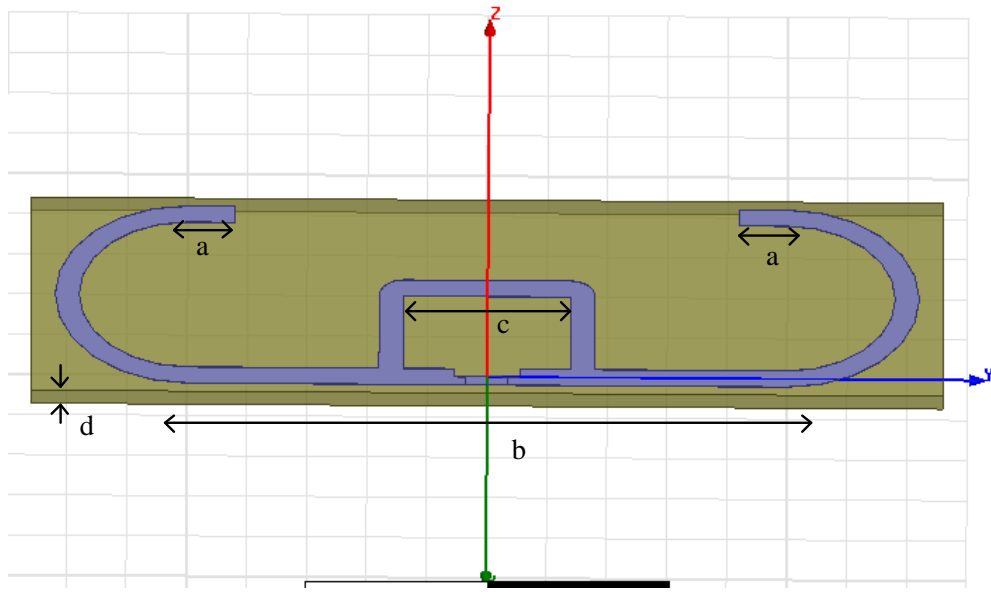


Figure 30: Antenna structure of Zero Power sensor platform.

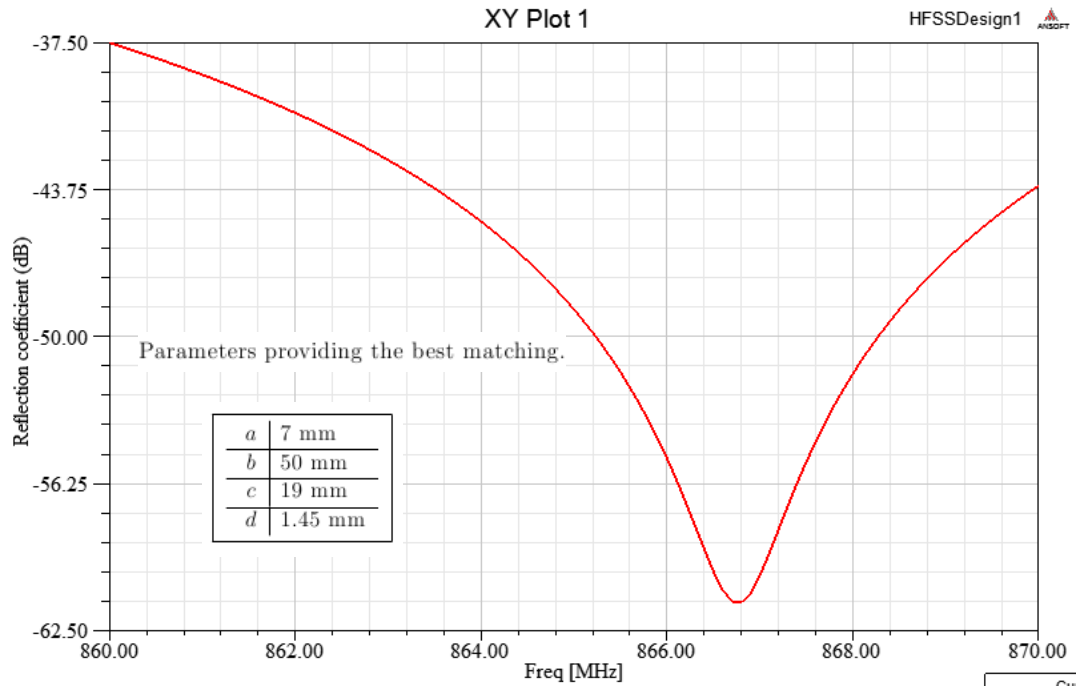


Figure 31: Simulated antenna structure providing the best matching to Zero Power sensor impedance.

Antenna impedance is simulated using different values for parameters  $a$ ,  $b$ , and  $c$ . The best matching and the parameters for the best matching are shown in Fig.

31. The simulated antenna impedance for this antenna structure is  $12.98 + j212.44 \Omega$ . Fig. 32 shows the 3D plot of antenna gain, which is 1.97 dB at the direction of Z-axis. The antenna structure is manufactured at VTT and a photograph of it is shown in Fig. 33.

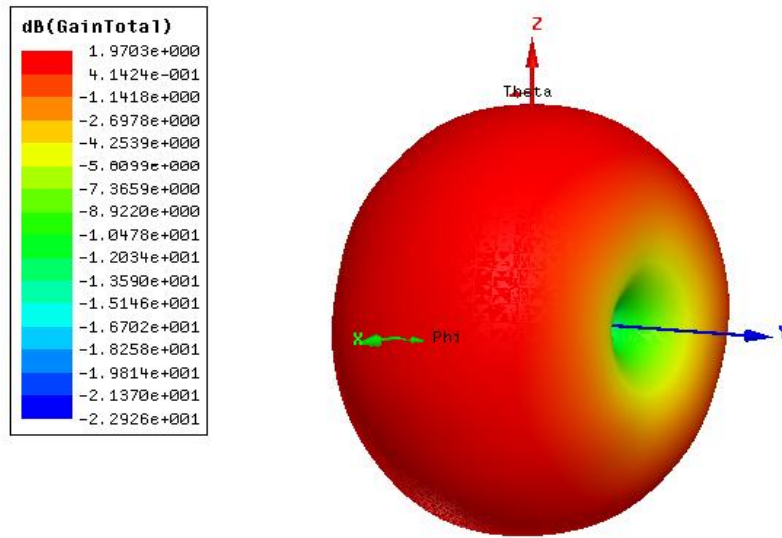


Figure 32: 3D plot of the Zero Power antenna gain.

Measurement of the antenna impedance with a VNA turned out to be challenging because the antenna is a balanced structure while VNA port is unbalanced. First we used a quarter-wave balun, which is shown in Fig. 33. Because the balun is not



Figure 33: Photograph of the Zero Power sensor antenna.

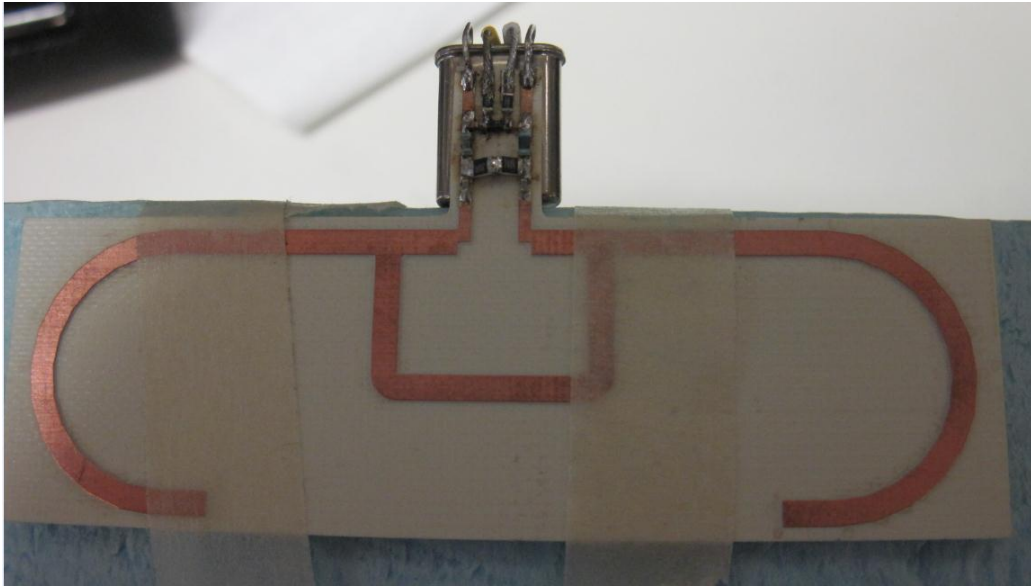


Figure 34: Photograph of the optimized sensor prototype.

designed exactly for 866 MHz and there is still part of the cable not shielded by the balun, the measured impedance did still not match exactly to the simulated one. Since we do not have the right instrument to measure the impedance, we decide to rely on simulations and characterize the sensor performance by the intermodulation response measurements afterwards. Finally, the sensor platform and the antenna are combined together and manufactured, which is shown in Fig. 34.

## 5 Performance of the optimized Zero Power sensor

### 5.1 Measurement setup

The measurement setup for the optimized Zero Power sensor is shown in Fig. 35.

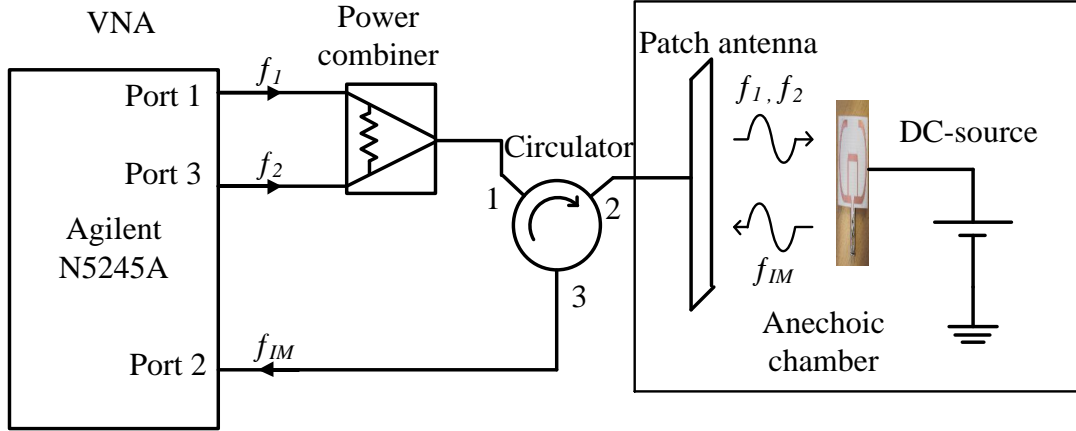


Figure 35: Schematic layout of the optimized Zero Power sensor prototype.

The fundamental tones at  $f_1$  and  $f_2$  fed from Port 1 and Port 3 of the VNA (Agilent, N5245A) are combined together with the power combiner (Mini-Circuits, ZFSC-2-2-S), and then fed to the reader patch antenna (Standard Patch Antenna 800-1000 MHz) through the circulator (Voyantic, Circulator V2.0). The intermodulation signal reflected from the sensor is received by the reader patch antenna then fed to Port 2 of the VNA through the circulator. A photograph of the wireless measurement is shown in Fig. 36. Table 4 collects all the parameters of the measurement setup for the optimized Zero Power sensor.

### 5.2 Fitting of the capacitance of the varactor

SKYWORKS SMV1413-079LF is chosen to be the capacitive sensor element to obtain the best read-out resolution. The voltage-dependent junction capacitance is obtained by fitting (3.7) to the  $C$ - $V$  values of the data sheet [45].  $C$ - $V$  values of the data sheet are shown with the fitted model in Fig. 37.

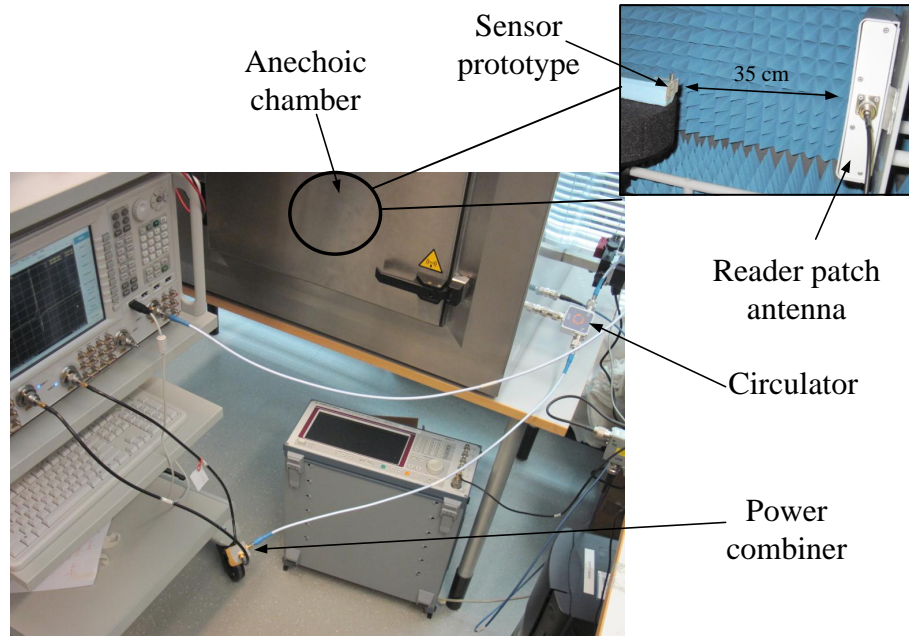


Figure 36: Photograph of the measurement setup for the optimized Zero Power sensor.

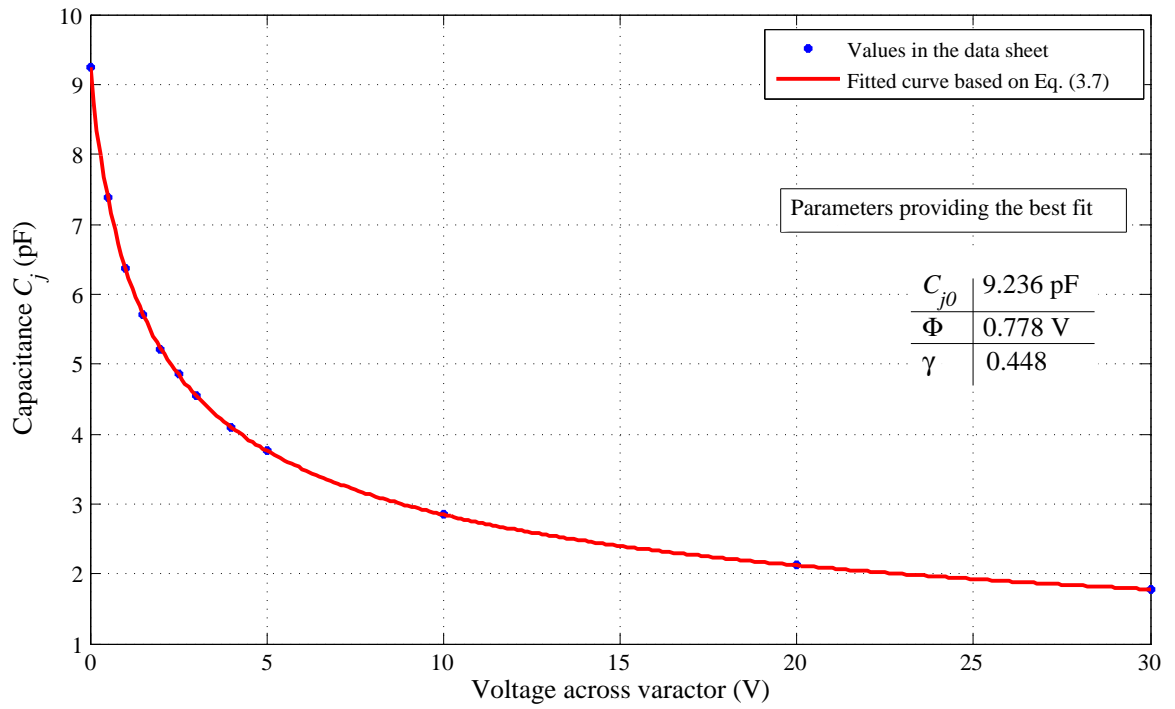


Figure 37: Fitted capacitance as a function of voltage across the varactor.

Table 4: Measurement parameters for the optimized Zero Power sensor prototype.

|  |   |
|--|---|
| 1st Fundamental frequency                                | $f_1 = 895 \text{ MHz}$   |
| 2nd Fundamental frequency                                | $f_2 = 896.99 \text{ MHz} \dots$<br>$\dots 897.01 \text{ MHz}$  |
| Difference frequency                                     | $f_\Delta = 1.99 \text{ MHz} \dots$<br>$\dots 2.01 \text{ MHz}$ |
| Oscillation frequency of the quartz crystal              | $f_o = 2 \text{ MHz}$   |
| Input power  | $P_1 = P_2 = 10 \text{ dBm}$                                    |
| Bias voltage   | $V_j = 0 \text{ V} \dots 30 \text{ V}$                          |
| Bias voltage step  | $V_{step} = 0.1 \text{ V}$                                      |
| Wavelength   | $\lambda = 0.335 \text{ m}$                                     |
| Transmitted power  | $P_t = 24 \text{ dBm}$  |
| Reader patch antenna gain                                | $G_r = 8 \text{ dBi}$   |
| Sensor antenna gain                                      | $G_s = 1.97 \text{ dBi}$  |
| Distance between the sensor prototype and reader antenna | $d = 35 \text{ cm}$   |
| Noise power  | $P_{Noise} = -120 \text{ dBm}$                                  |

### 5.3 Experiments of the optimized Zero Power sensor

#### 5.3.1 Carrier frequency sweep

Matching between the antenna and the sensor is studied by measuring the IM response at different carrier frequencies. In these measurements, the sensor is unbiased and the difference frequency is kept  $f_\Delta = 2 \text{ MHz}$ . The best matching is obtained at 895 MHz (see Fig. 38).

#### 5.3.2 Intermodulation response as a function of difference frequency

Capacitance sensitivity of the sensor is studied by measuring the sensor responses with differently biased varactor. The varactor is biased with voltages from 0 V to 30 V, at a step of 0.1 V. In Fig. 39, all the samples has been partial enlarged arround the resonance frequency. From Fig. 39, the same law of the frequency shift caused by the bias voltage is observed as in case of the previous prototypes.

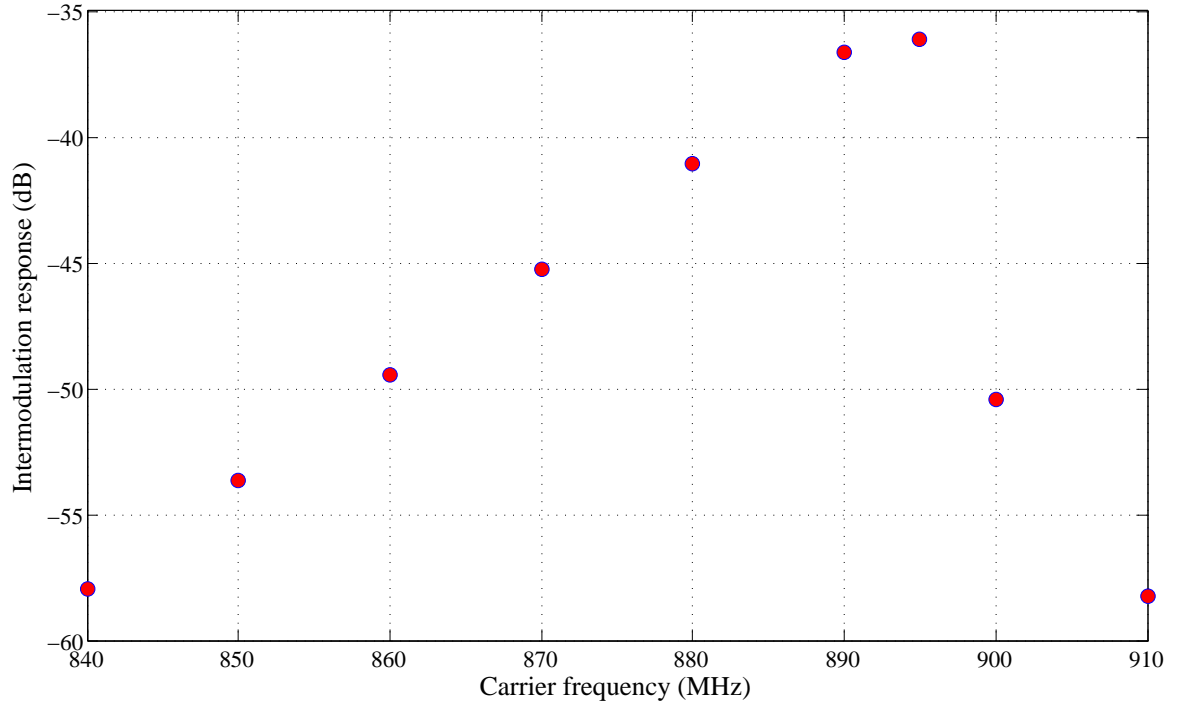


Figure 38: Matching of the sensor platform and antenna at different carrier frequencies.

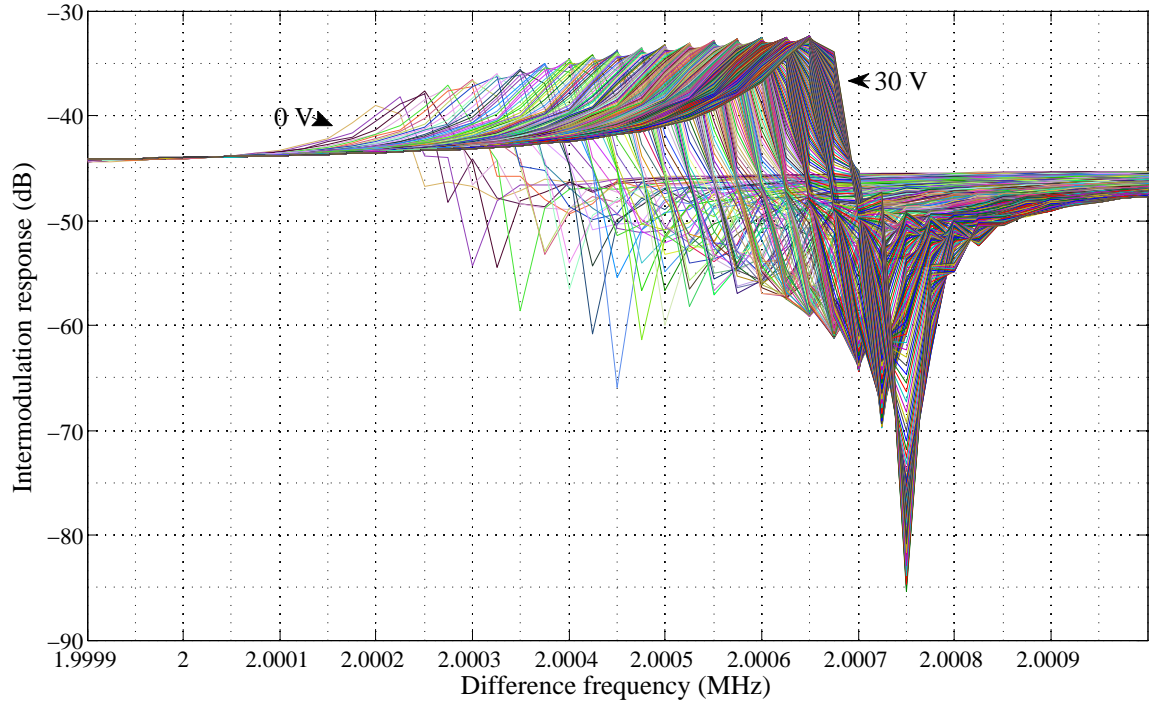


Figure 39: Intermodulation response at frequency  $f_{\Delta}$  as a function of bias voltages.

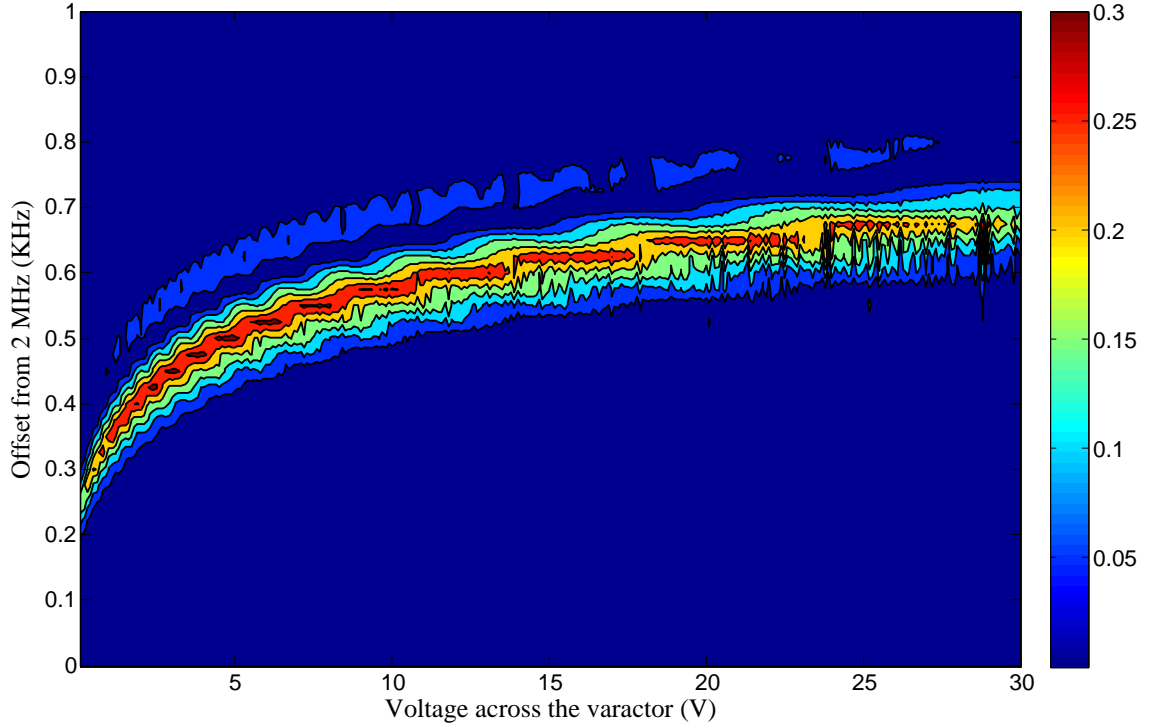


Figure 40: 2D plot of intermodulation sensitivity as a function of the voltage across the varactor ( $X$ -axis) and the offset from 2 MHz ( $Y$ -axis).

### 5.3.3 Intermodulation sensitivity

The intermodulation sensitivity  $|\frac{dS_{IM}(ref)}{dC_s}C_s|$  is calculated and plotted. Fig. 40. is a 2D plot of the intermodulation sensitivity as a function of the voltage across the varactor in  $X$ -axis and the intermodulation frequency in  $Y$ -axis. The white parts of the figure are the areas outside the resonance. As is shown in Fig. 40, the intermodulation sensitivity is very high at all bias voltages, and when the bias voltage is 4.9 V, the intermodulation sensitivity reaches its maximum, which is 0.3202. Table 5 is a comparison for the performance of the optimized sensor and 1.2 GHz prototype.

Table 5: Comparison for the optimized sensor and 1.2 GHz sensor.

|                             | Optimized Zero Power sensor | 1.2 GHz sensor |
|-----------------------------|-----------------------------|----------------|
| Intermodulation sensitivity | 0.3202                      | 0.19           |



From the result, the intermodulation sensitivity is about 68% higher than that of the previous 1.2 GHz sensor. Hence, it can be concluded that the optimization of the Zero Power sensor is successful.

## 5.4 Read-out resolution

Let us assume a measurement in free space. Since the difference of the intermodulation resolution at different distances is only caused by the FSPL (Free Space Path Loss), there is no need to repeat the measurement at all distances. Instead, the intermodulation resolution can be predicted by using the measured intermodulation response.

By substituting the intermodulation sensitivity and the parameters in Table 4 into (3.22), the achievable read-out resolution is calculated and plotted in Fig. 41.

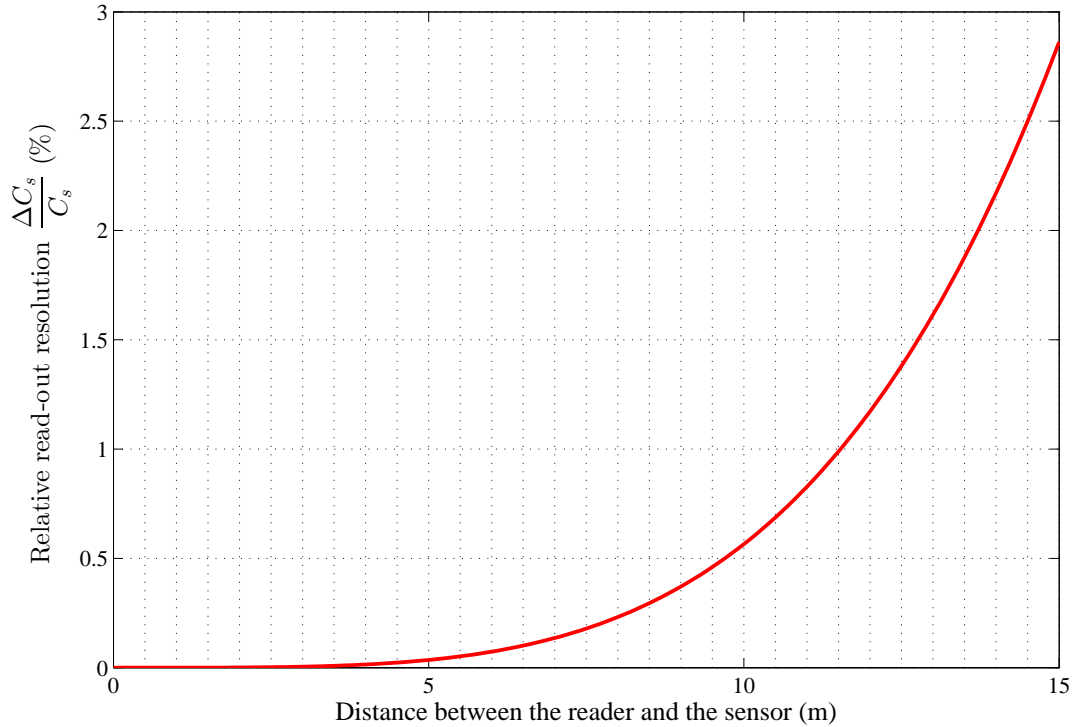


Figure 41: Read-out resolution of the optimized Zero Power sensor.

The achievable read-out resolution in Fig. 41 shows that when the distance increases up to 13 meters, 1 % change of the capacitance can still be detected. Note

that even higher resolution can be achieved using other antennas or more sensitive reader device.

## 5.5 ECG measurement

A wireless ECG (Electrocardiography) measurement is demonstrated with the sensor. The heartbeat generates a small voltage on the skin of the chest (several millivolts), which changes the capacitance of the varactor and the output of the intermodulation response.

Fig. 42 shows the ECG measurement setup. The sensor is located in the anechoic chamber, and two copper patches are attached to the human body near the heart. The reader VNA setup is kept the same as in the previous measurement for the optimized sensor except that the time domain is used so that the heartbeat can be recorded directly in time.

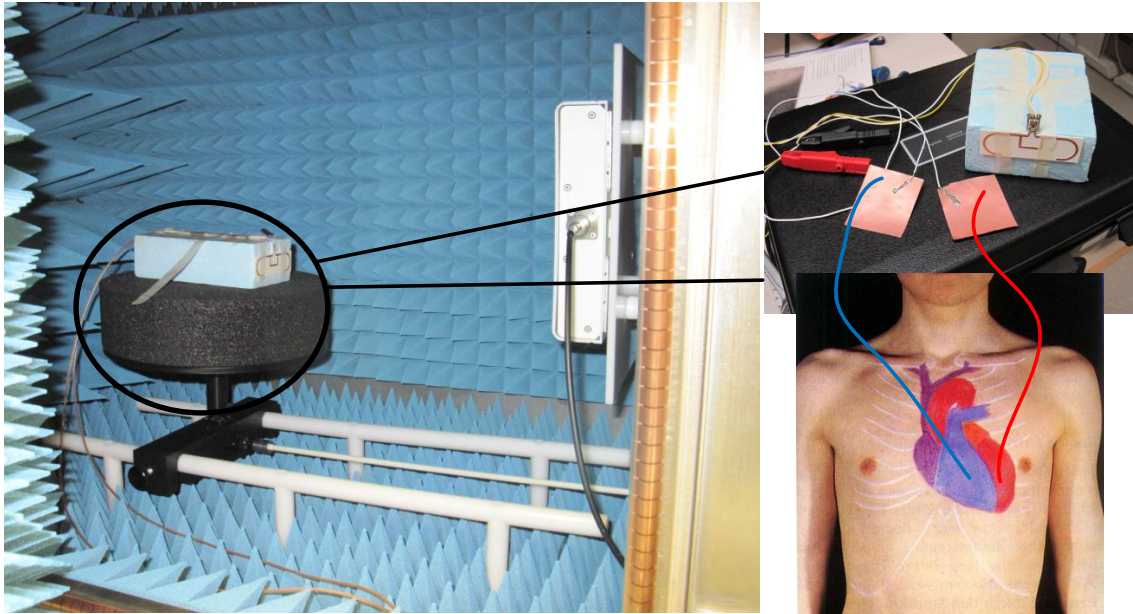


Figure 42: ECG measurement setup.

Fig. 43 shows the heartbeat of the Author and another subject (Juho) during 10 seconds, and Fig. 44 illustrates the heartbeat of the Author during 60 seconds. Fig. 45 shows the same ECG signal as in Fig. 44 after a digital high-pass filter used

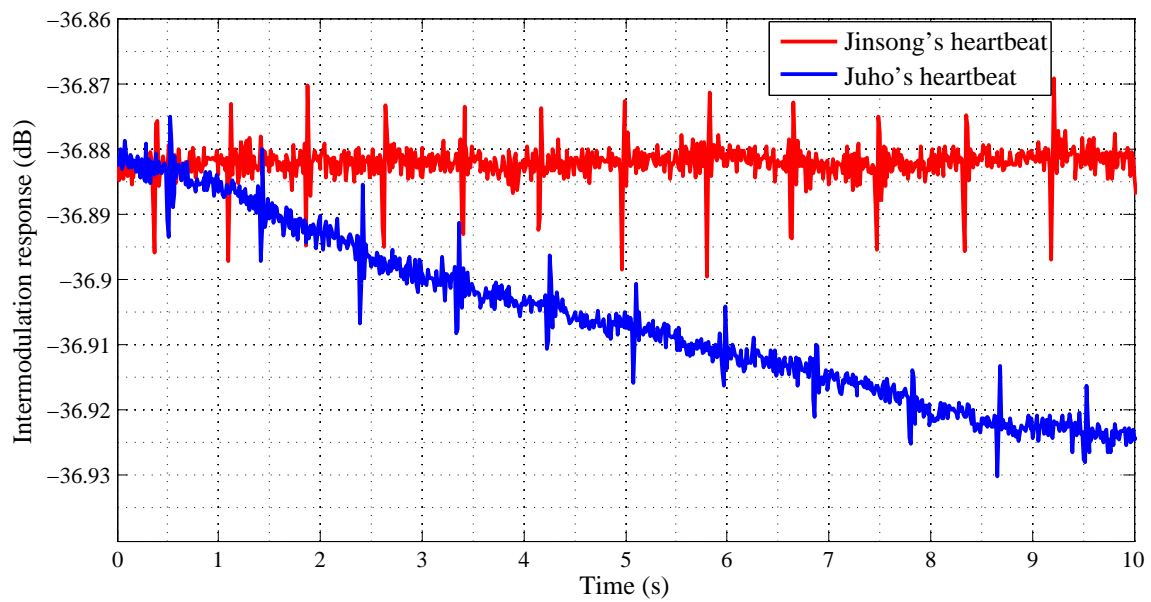


Figure 43: Measured heartbeat in 10 seconds.

to filter out slow variations due to respiration and other muscular activities.

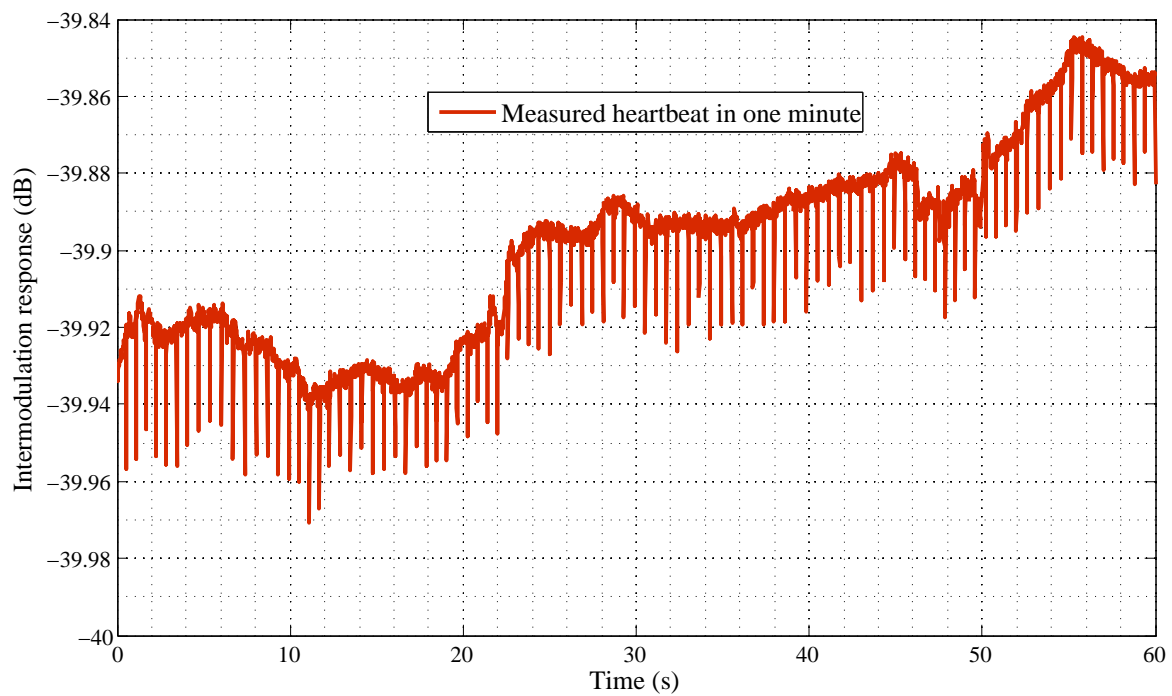


Figure 44: Measured heartbeat in one minute.

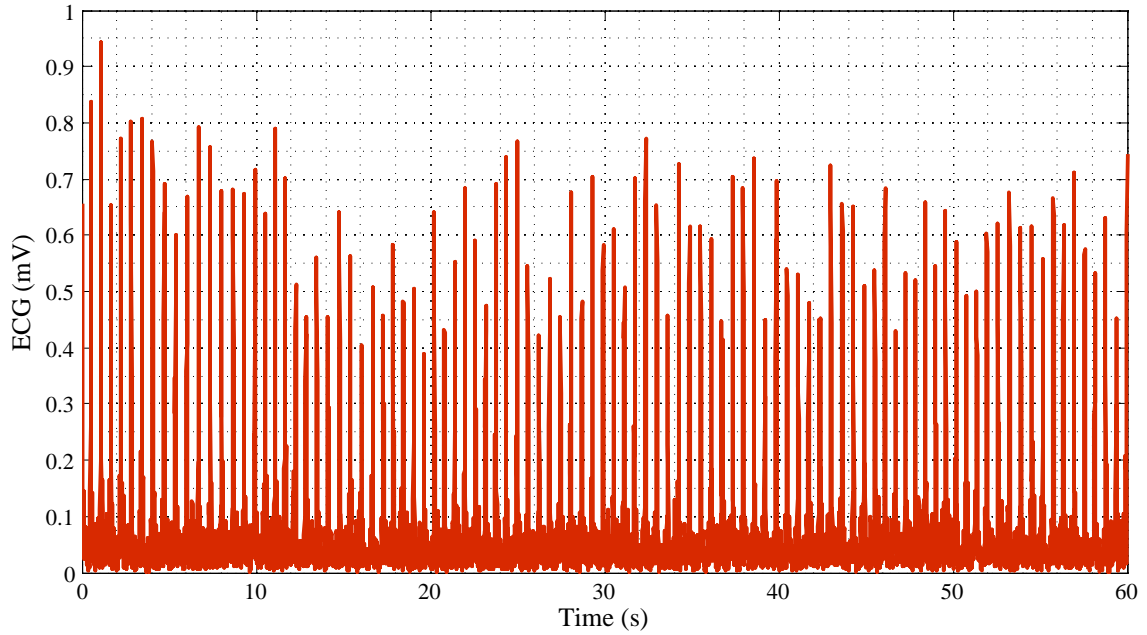


Figure 45: ECG signals in one minute.

HRV (Heart Rate Variability) is a physiological phenomenon where the time interval between heart beats varies. HRV is found to correlate with physical and mental stress. It is measured by the variation in the beat to beat interval. The heartbeat interval is plotted in Fig. 46. Hence, HRV can be calculated as the time difference between heart beats, which is show in Fig. 47. The result demonstrates that the sensor can be used also for wireless HRV measurements.

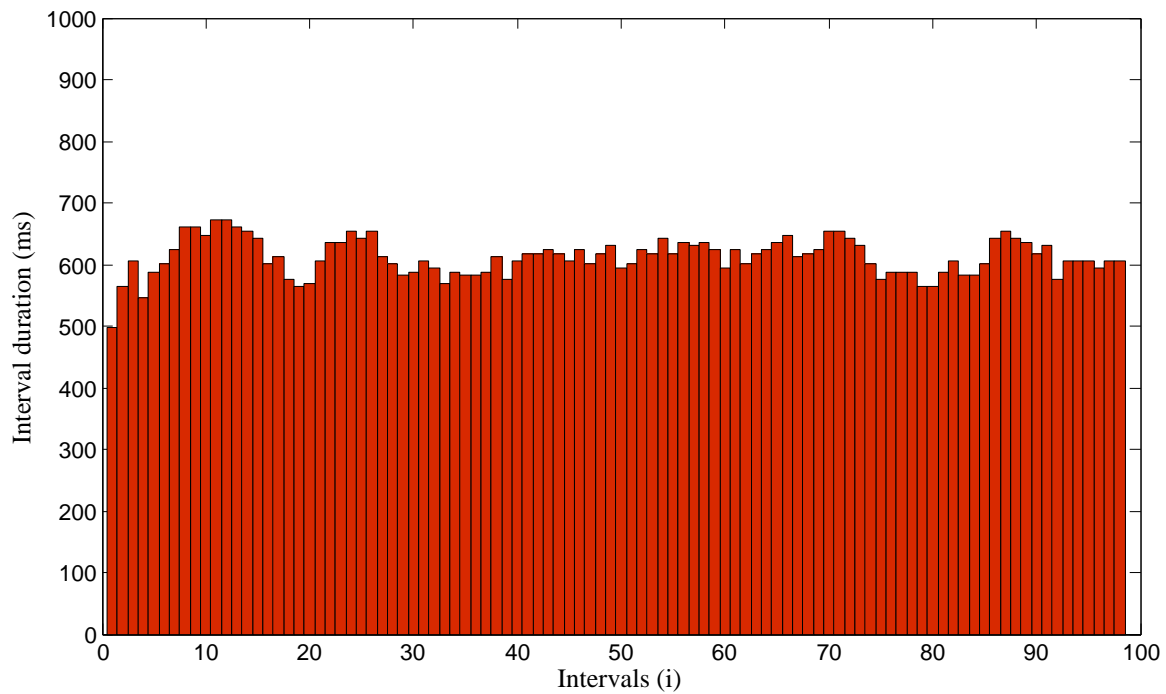


Figure 46: Heart rate intervals in one minute.

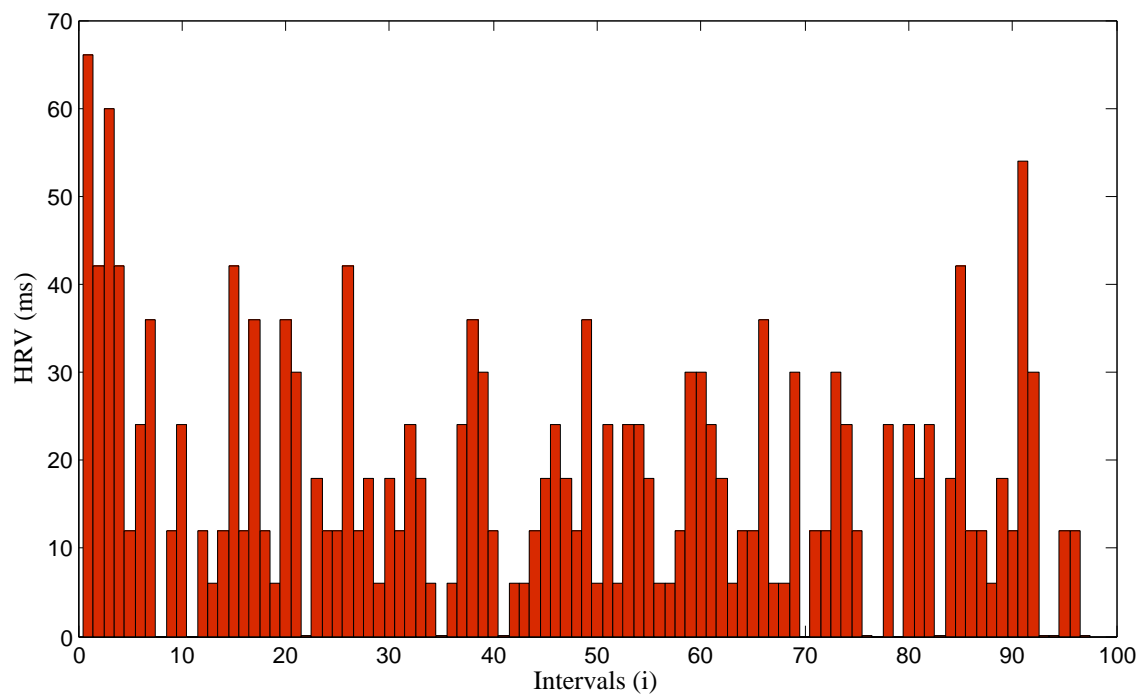


Figure 47: HRV signals in one minute.

## 6 Conclusion

In this thesis work, theoretical basis for the working principle of the Zero Power sensor is reviewed, and a theory to predict the read-out resolution is established. Based on the theory, the first wired sensor prototypes are manufactured and experimentally characterized. The achievable read-out resolution is theoretically predicted for the first time. The measurement and the prediction shows that the sensor based on the intermodulation principle can offer a large read-out distance and good resolution required in the Zero Power project to which this thesis contributes.

The optimization theory of the sensor circuit is established and the optimized values for the capacitances and inductances are obtained. New prototypes with the optimized circuit are fabricated. Conjugate matched antenna for the sensor is optimized and manufactured. The intermodulation response is measured wirelessly and the sensitivity of the optimized sensor prototype is experimentally characterized and compared with that of the first prototype. The comparison shows that the performance of the optimized sensor improves 68% as compared to the first prototype. The achievable read-out resolution is predicted using the measured intermodulation response of the optimized sensor. Finally, ECG measurement is given as one example for the possible applications of the Zero Power sensor. ECG signals are measured wirelessly, which shows the sensor is sensitive enough for ECG signals and could be used for HRV monitoring.

In the near future, a sensor antenna with high gain will be designed such that the resolution can be further improved, and different sensor elements can be plugged in to fulfill different sensing fields (e.g. pressure, temperature). In the final stage, the sensor can be integrated into MEMS (microelectromechanical systems) so the size of the sensor will be highly reduced.

## References

- [1] D. Estrin, L. Girod, G. Pottie, and M. Srivastava, "Instrumenting the world with wireless sensor networks," in *Proc. IEEE Int. Conf. Acoust., Speech, Signal Process. (ICASSP)*, Salt Lake City, UT, May 2001, vol. 4, pp. 2033–2036.
- [2] P. Corke, T. Wark, R. Jurdak, R. Moore, and P. Valencia, "Environmental wireless sensor networks," *Proceedings of the IEEE*, vol. 98, no. 11, pp. 1903–1917, 2010.
- [3] R. Weinstein, "RFID: A technical overview and its application to the enterprise," *IT Prof.*, vol. 7, no. 3, pp. 27–33, May/Jun. 2005.
- [4] W. Chen, J.C. Hou, and L. Sha, "Dynamic clustering for acoustic target tracking in wireless sensor networks," *IEEE Trans. Mobile Computing*, vol. 3, no. 3, pp. 258–271, Jul./Aug. 2004.
- [5] OMEGA Engineering Technical Reference, [Online]. Available: <http://www.omega.com/prodinfo/wirelessensors.html>
- [6] M.P. da Cunha, R.J. Lad, P. Davulis, A. Canabal, T. Moonlight, S. Moulzolf, D.J. Frankel, T. Pollard, D. McCann, E. Dudzik, A. Abedi, D. Hummels, and G. Bernhardt, "Wireless acoustic wave sensors and systems for harsh environment applications," in *Proc. IEEE WiSNet*, 2011, pp. 41–44.
- [7] J. English and M. Allen, "Wireless micromachined ceramic pressure sensors," in *Proc. 12th IEEE Microelectromech. Syst. Conf.*, Orlando, FL, 1999, pp. 511–516.
- [8] B. Dixon, V. Kalinin, J. Beckley, and R. Lohr, "A second generation in-car tire pressure monitoring system based on wireless passive SAW sensors," *Proceedings of 2006 IEEE Frequency Control Symposium and Exposition*, 2006, pp. 374–380.
- [9] R. Angeles, "RFID technologies: Supply-chain applications and implementation issues," *Inform. Syst. Managem.*, vol. 22, pp. 51–65, 2005.

- [10] G. Werner-Allen, K. Lorincz, M. Welsh, O. Marcillo, J. Johnson, M. Ruiz, and J. Lees, "Deploying a wireless sensor network on an active volcano," *IEEE Internet Computing*, vol. 10, no. 2, pp. 18–25, Mar./Apr. 2006.
- [11] T. Sivanadyan and A. Sayeed, "Active wireless sensing for rapid information retrieval in sensor networks," in *Proc. 5th Int. Conf. Information Processing in Sensor Networks (IPSN)*, Apr. 2006, pp. 85–92.
- [12] Z. Hu and B. Li, "On the fundamental capacity and lifetime limits of energy-constrained wireless sensor networks," in *Proceedings of 10th IEEE Real-Time and Embedded Technology and Applications Symposium (RTAS 2004)*, Toronto, Canada, May 2004, pp. 25–28.
- [13] TagSense, [Online]. Available: [http://www.tagsense.com/index.php?option=com\\_content&view=category&layout=blog&id=50&Itemid=118](http://www.tagsense.com/index.php?option=com_content&view=category&layout=blog&id=50&Itemid=118)
- [14] R. Jedermann, L. Ruiz-Garcia, and W. Lang, "Spatial temperature profiling by semi-passive RFID loggers for perishable food transportation," *Comput. Electron. Agric.*, vol. 65, pp. 145–154, 2009.
- [15] N. Cho, S.J. Song, S. Kim, and H.J. Yoo, "A 5.1- $\mu$ W UHF RFID tag chip integrated with sensors for wireless environmental monitoring," *ESSCIRC 2005: Proceedings of the 31st European Solid-State Circuits Conference*, Grenoble, France, 2005, pp. 279–282.
- [16] A. Vergara, E. Llobet, J.L. Ramírez, P. Ivanov, L. Fonseca, S. Zampolli, A. Scorzoni, T. Becker, S. Marco, and J. Wöllenstein, "An RFID reader with onboard sensing capability for monitoring fruit quality," in *Eurosenors 2006*, Goteborg, Sweden, 2006.
- [17] K. Finkenzeller, *RFID Handbook*, Munich, John Wiley & Sons Inc., 2003.
- [18] V. Viikari, H. Seppä, and D. Kim, "Intermodulation read-out principle for passive wireless sensors," *IEEE Transactions on Microwave Theory and Techniques*, vol. 59, no. 4, pp. 1025–1031, Apr. 2011.



- [19] V. Viikari and H. Seppä, “Passive wireless sensor platform utilizing a mechanical resonator,” Manuscript submitted for publication in *IEEE Sensors*.
- [20] R. Want, “Enabling ubiquitous sensing with RFID,” *Computer*, vol. 37, no. 4, pp. 84–86, April 2004.
- [21] A. Lehto, J. Nummela, L. Ukkonen, L. Sydanheimo, and M. Kivikoski, “Passive UHF RFID in paper industry: Challenges, benefits and the application environment,” *IEEE Trans. Autom. Sci. Eng.*, vol. 6, no. 1, pp. 66–79, Jan. 2012.
- [22] L. Li and F. Kong, “Research on assembly quality tracing of automobile industry based on RFID,” *Advanced Technology of Design and Manufacture*, Beijing, Nov. 2010, pp. 498–503.
- [23] A.P. Sample, D.J. Yeager, P.S. Powledge, A.V. Mamishev, and J.R. Smith, “Design of an RFID-based battery-free programmable sensing platform,” *IEEE Transactions on Instrumentation and Measurement*, vol. 57, no. 11, pp. 2608–2615, Nov. 2008.
- [24] A. Pohl, “A review of wireless SAW sensors,” *IEEE Trans. Ultrason., Ferroelect., Freq. Contr.*, vol. 47, no. 2, pp. 317–332, Mar. 2000.
- [25] G. Scholl, F. Schmidt, T. Ostertag, L. Reindl, H. Scherr, and U. Wolff, “Wireless passive SAW sensor systems for industrial and domestic applications,” in *IEEE International Frequency Control Symposium 1998*, May 1998, pp. 595–601.
- [26] G. Frye, R. Kottenstette, E. Heller, J. Brinker, S. Casalnuovo, A. Sellinger, N. Raman, and Y. Lu, “Optimizing surface acoustic wave sensors for trace chemical detection,” *Proc. IEEE Transducers '97*, 1997, vol. 2, pp. 1323–1326.
- [27] J.C. Butler, A.J. Vigliotti, F.W. Verdi, and S.M. Walsh, “Wireless, passive, resonant-circuit, inductively coupled, inductive strain sensor,” *Sens. Actuators A, Phys.*, vol. 102, no. 1–2, pp. 61–66, Dec. 2002.

- [28] R. Nopper, R. Niekrawietz, and L. Reindl, "Wireless readout of passive LC sensors," *IEEE Trans. Instrum. Meas.*, vol. 59, no. 9, pp. 2450–2457, Sep. 2010.
- [29] S. Bhadra, G.E. Bridges, D.J. Thomson, and M.S. Freund, "A wireless passive sensor for pH monitoring employing temperature compensation," *2011 IEEE Sensors*, Oct. 2011, pp. 1522–1525.
- [30] V. Viikari, J. Chisum, and H. Seppä, "Wireless passive photo detector for insect tracking," *Microw. Opt. Technol. Lett.*, vol. 52, no. 10, pp. 2312–2315, Oct. 2010.
- [31] B.G. Colpitts and G.Boiteau, "Harmonic radar transceiver design: Miniature tags for insect tracking," *IEEE Trans. Antennas Propag.*, vol. 52, no. 11, pp. 2825–2832, Nov. 2004.
- [32] H. Staras and J. Shefer, "Harmonic radar detecting and ranging system for automotive vehicles," U.S. Patent 3 781 879, Jun. 30, 1972.
- [33] Glcharvat, [Online]. Available: [http://www.glcharvat.com/Dr.\\_Gregory\\_L.\\_Ch-arvat\\_Projects/Harmonic\\_Radar.html](http://www.glcharvat.com/Dr._Gregory_L._Ch-arvat_Projects/Harmonic_Radar.html)
- [34] D. Psychoudakis, W. Moulder, C.C. Chen, H. Zhu, and J. L. Volakis, "A portable low-power harmonic radar system and conformal tag for insect tracking," *IEEE Antennas and Wireless Propagation Letters*, vol. 7, pp. 444–447, 2008.
- [35] M. Bouthinon, J. Gavan, and F. Zadworny, "Passive microwave transposer, frequency doubler for detecting the avalanche victims," *10th European Microwave Conference*, Warszawa, Poland, Sep. 1980, pp. 579–583.
- [36] D.E.N. Davies and R.J. Klensch, "Two-frequency secondary radar incorporating passive transponders," *Electron. Lett.*, vol. 9, no. 25, pp. 592–593, Dec. 1973.

- [37] V. Viikari, H. Seppä, T. Mattila, and A. Alastalo, “Wireless ferroelectric resonating sensor,” *IEEE Trans. Ultrason., Ferroelect., Freq. Control*, vol. 57, no. 4, pp. 785–791, Apr. 2010.
- [38] G. Massobrio and P. Antognetti, *Semiconductor Device Modeling with SPICE*, 1st ed., New York: McGraw-Hill, Dec. 1998.
- [39] BB149A Data Sheet, [Online]. Available: [http://www.nxp.com/documents/data\\_sheet/BB149A.pdf](http://www.nxp.com/documents/data_sheet/BB149A.pdf)
- [40] D.M. Pozar, *Microwave Engineering*, 3rd ed., New York: John Wiley & Sons Inc., 2005.
- [41] H. Jiang, D.S. Shin, G.L. Li, T.A. Vang, D.C. Scott, and P.K.L. Yu, “The frequency behavior of the third-order intercept point in a waveguide photodetector,” *IEEE Photon. Technol. Lett*, vol. 12, pp. 540–542, 2000.
- [42] C.A. Balanis, *Antenna Theory*, New York: John Wiley & Sons Inc., 2003.
- [43] J. Rahola, “Power waves and conjugate matching,” *IEEE Trans. Circuits Sys. II, Exp. Briefs*, vol. 55, no. 1, pp. 92–96, Jan. 2008.
- [44] K.V.S. Rao, P.V. Nikitin, and S.F. Lam, “Antenna design for UHF RFID Tags: A review and a practical application,” *IEEE Trans. Antennas and Propagation*, vol. 53, no. 12, pp. 3870–3876, 2005.
- [45] SKYWORKS SMV1413 Data Sheet, [Online]. Available: <http://www.datasheetcatalog.org/datasheet2/7/0tya37k1uf8fjwy2jck2ts25qscy.pdf>